

SCUOLA DI INGEGNERIA E ARCHITETTURA

-Campus di Forlí -

Master's Degree in Aerospace Engineering class LM20

Graduation Thesis in:
Experimental Aerodynamics

OPTICAL ANALYSIS OF TURBULENT SUPERSTRUCTURES IN THERMAL CONVECTION USING TEMPERATURE SENSITIVE PAINT

Candidate: Supervisor:

Alessandro Bo Prof. Gabriele Bellani

Examiner: Co-Supervisors:

Dr. Ing. Marco Costantini Dr. Johannes Bosbach

Dr. Stephan Weiss

Graduation Session of October 2025 Academic Year 2024/2025 In collaboration with:



Contents

1	Introduction					
	1.1	Aim o	of the thesis	4		
2	Theoretical background					
	2.1	Raylei	igh-Bénard convection	7		
	2.2	erature sensitive paint	13			
		2.2.1	Photonics and temperature evaluation	13		
		2.2.2	Typical TSP experimental setup	15		
3	Exp	erime	ntal setup	17		
	3.1	Raylei	igh-Bénard experiment	17		
	3.2	Exper	imental procedure	19		
	3.3	Uncer	tainty analysis and measurement accuracy	20		
		3.3.1	Temporal and spatial resolution	21		
		3.3.2	Assessment of temperatures	22		
		3.3.3	Rayleigh number	23		
		3.3.4	Nusselt number	23		
		3.3.5	Biot number	25		
		3.3.6	Richardson number	25		
		3.3.7	Stability of TSP in water	26		
		3.3.8	Transient intensity evolution	28		
4	Dat	a proc	cessing	33		
	4.1	1 Temperature Calibration				
		4.1.1	General Remarks	33		
		4.1.2	Absolute temperature calibration	34		
		4.1.3	Relative temperature calibration	35		
		4.1.4	Spatial calibration	37		
	4.2	Image	Processing	37		
		4.2.1	Pre-processing	37		

iv	CONTENTS

		4.2.2 Intensity to temperature conversion	40			
5	Results					
	5.1	Main flow features	43			
		5.1.1 Instantaneous temperature fields	43			
		5.1.2 Averaged temperature fields	46			
	5.2	Statistical analysis	48			
	5.3	Comparison with other measurements and DNS	49			
	5.4	Final discussion and summary	51			
6	Conclusions					
\mathbf{A}	A Appendix					

Acknowledgements

This thesis marks the culmination of three years of a university path that has taught me far more than I ever expected and will always stay with me wherever I go. It has been a challenging yet deeply rewarding adventure, that I would gladly repeat without hesitation. And though this journey was not always easy, I was never alone.

First of all, I wish to express my gratitude to my supervisor, Professor Gabriele Bellani, who has supported me not only throughout this thesis but also during previous stages of my academic career. Thank you for being my first point of contact between myself and DLR, and for introducing me to the research team, opening the door to this experience.

A heartfelt thanks goes to my supervisors at DLR Göttingen, Dr. Johannes Bosbach and Dr. Stephan Weiss, for their guidance and for organising a thesis that encompassed every aspect of experimental research: planning of the experiment, its execution, troubleshooting, data processing, and analysis. Thank you for actively involving me in every stage of the process, even those that extended beyond the duration of my stay at DLR. Thank you to Johannes for your patience and for the countless hours of discussion, first on the experiments and data, and later on the writing and structure of this thesis, and thank you for always motivating me to aim for excellence. Thank you to Stephan for your expert assistance in setting up the experiment, the measurement chain, and for your support in the theoretical aspects of RBC and on the thesis writing.

Another thank you goes to the colleagues in the TSP/PSP group for their support during the preparation of the measurement campaigns and throughout the data analysis phase. In particular, I would like to thank C. Klein, U. Henne, D. Yorita, B. Dimond, M. Costantini, and J. Lemarechal for their technical expertise, collaboration, and constant willingness to help. I also extend my gratitude to all the colleagues at DLR and the people I met during the PSP/TSP course and PIV course, for all the fruitful talks that made this thesis something I am very proud of. A great thank you goes to the cities of Forlì and Göttingen, which have been my homes over the past three years, and through which I had the privilege of meeting

vi CONTENTS

people from over 60 different countries. I am grateful to all my friends, who stood by me, supported me, and walked alongside me through this journey. Last but not least, I want to thank my family, who have been by my side through these years of change and difficult decisions, as well as in happy moments and celebrations, even though I was distant.

Abstract

Rayleigh-Bénard convection (RBC) refers to a family of flows generated in a horizontally extended volume with adiabatic sidewalls, wherein the fluid is uniformly heated from below and cooled from above. The resulting fluid motion depends on the system's Rayleigh number (Ra), Prandtl number (Pr), and aspect ratio ($\Gamma = \frac{L}{H}$) between the lateral extension L and the height of the fluid layer H. Typical for the turbulent regime under strong thermal driving is the occurrence of coherent large-scale structures. Specifically, at small Γ , the flow is dominated by "Large-Scale Circulations" (LSC), which involve strong sidewall interactions. At higher Γ , as sidewall effects become negligible, so-called "Turbulent Superstructures" (TSS) evolve.

This study addresses the long-term development of temperature fields in RBC using a shallow water tank with a heated aluminium base and a water-cooled glass top plate. Variable sidewalls allow the control of Γ (ranging from 4 to 32). With an experimental setup incorporating temperature sensitive paint (TSP) with associated UV-LED illumination ($\lambda_{ab} \sim 395$ nm) and CCD camera, TSS were observed and studied via their thermal footprint on the top plate for Ra in the range $2.6 \times 10^4 < Ra < 1.2 \times 10^8$.

The application of TSP to slowly evolving flows like RBC, with the paint submerged in water for extended periods, represents an innovation in experimental fluid dynamics and comes along with novel challenges. The thesis, carried out at the Department of Experimental Methods within the Institute of Aerodynamics and Flow Technology at DLR Göttingen, Germany, aims to address these challenges and improve the accuracy of the measurements. The work primarily focuses on the development of an accurate calibration method to convert TSP intensity data to temperature. A preliminary analysis of temperature fields is also conducted, including the investigation of the transition from LSC to TSS, achieved by analysis of Probability Density Function (PDF) of temperature fluctuations.

Chapter 1

Introduction

Thermal convection, a process occurring whenever heat transfer involves fluid motion driven by a temperature gradient, is observed in numerous natural contexts. Examples range from everyday situations like a pot full of water on the stove or a cup of coffee, to large-scale phenomena such as convection in the atmosphere, the oceans, and in the outer core of the Earth and the Sun. Furthermore, thermal convection is a concept widely known in industrial applications such as fluid handling and mixing, ventilation systems, furnaces, and refrigeration units. In many of these cases, the temperature gradient is sufficiently large to induce turbulent flow.

Although thermal convection has been studied for over a century, the first quantitative optical experiment was performed by Bénard [1] in 1901 and further theoretically described by Rayleigh [2] in 1916. This classical system, employing a container of defined geometry (typically cylindrical or cuboidal), and enclosed between two horizontal plates, where the lower plate is uniformly heated and the upper plate is cooled, is now referred to as Rayleigh-Bénard convection (RBC). For some systems, the ones with large horizontal dimension compared to their height, the turbulent flow displays an organisation into prominent, persistent flow patterns known as turbulent superstructures (TSS). Conversely, in systems where the horizontal and vertical dimension are of the same order of magnitude, the flow organises into a single convection roll, which spans the entire domain. This roll, often called large scale circulation (LSC), shows rather complex dynamics, such as a diffusive change of orientation or random cessations and subsequent reorganisation.

RBC has been optically investigated experimentally using mostly shadowgraphy, Schlieren imaging and interferometry [3] and, in modern times, with techniques such as stereo particle image velocimetry (PIV) and particle tracking velocimetry (PTV). While high-density particle tracking nowadays allows for volumetric velocity field measurements, a similar technique to measure the temperature field at the surface

4 1. INTRODUCTION

of one of the horizontal plates does not exist. Instead, temperature is typically measured just at few locations via thermally-sensitive electrical resistors (thermistors). This limitation motivates the application of temperature sensitive paint (TSP) in the present study. TSP is an optical measurement technique utilising a phosphorescent dye embedded within a matrix material, applied as a coating to a surface. Upon illumination by a light source (typically a UV-LED) the coating exhibits luminescence whose intensity or lifetime depends on the temperature of the fluid in contact with the surface. This emission is captured by a camera, and after a calibration procedure, a temperature field can be obtained from the painted surface. In this way, TSP provides a non intrusive and spatially resolved method for surface temperature measurement that, employed to one of the horizontal plates in RBC, can provide valuable information on the shape of the thermal patterns, studying them via their imprint on the paint layer.

Due to its fast response to temperature changes, TSP is commonly employed in high-speed applications, such as high Reynolds number wind tunnels like the European Transonic Wind Tunnel (ETW) in Köln, or hypersonic facilities such as the High Enthalpy Shock Tunnel (HEG) in Göttingen. Moreover, the equipment used for capture TSP emission, such as LEDs and cameras, is typically utilised for experiments with acquisition times on the order of milliseconds to seconds. Therefore, its application to RBC represents an innovative approach, not only in terms of the flow regime but also from the perspective of the measurement technique itself.

The thesis begins with a theoretical overview of Rayleigh-Bénard convection and the operating principles of the TSP technique. This is followed by a detailed description of the experimental setup and an assessment of its measurement accuracy. The subsequent sections discuss the collected data, concluding with a brief outlook on the quantitative analysis performed.

1.1 Aim of the thesis

The work for this thesis was carried out at the Experimental Methods department within the Institute of Aerodynamics and Flow Technology at DLR Göttingen.

The specific objectives of this thesis were:

- Applying TSP to Rayleigh-Bénard convection for the measurement of temperatures at the top plate and the visualisation of flow structures.
- Assembling the experimental apparatus and performing of experiments for aspect ratios $\Gamma = 8$ and $\Gamma = 4$ as well as for different ΔT ;
- Assessing the stability of the TSP layer under operational conditions;

- Developing a calibration procedure for the TSP in this specific application, that takes into account time variations of the TSP luminescence intensity when exposed to water as well as fluctuations in LED illumination;
- Characterising the accuracy and the boundary conditions of the experimental setup;
- Implementing a measurement chain for quantitative data extrapolation;
- Conducting measurements in order to investigate the flow for different control parameters (aspect ratio and Rayleigh number).

Chapter 2

Theoretical background

2.1 Rayleigh-Bénard convection

Rayleigh-Bénard convection (RBC) is a thermally-driven flow that emerges when a fluid layer enclosed between parallel, horizontal plates is uniformly heated from below and cooled from above. When the applied temperature difference exceeds a critical value, a buoyancy-induced flow occurs, which can be highly coherent, chaotic or turbulent, depending on the governing parameters. Generally, with the resulting flow, heat is convected from the bottom to the top plate. The behaviour of RBC is typically characterised by a set of dimensionless parameters. The primary among these is the Rayleigh number (Ra), which relates the strength of the thermal driving to the damping by thermal and momentum diffusion. It is defined as

$$Ra = \frac{g\alpha\Delta TH^3}{\nu\kappa},\tag{2.1}$$

where $\Delta T = T_b - T_t > 0$ denotes the difference between the bottom (T_b) and the top plate (T_t) temperature, H the height of the fluid layer, g the gravitational acceleration, α the isobaric thermal expansion coefficient, ν the kinematic viscosity and κ the thermal diffusivity. Another governing parameter is the Prandtl number (Pr), which expresses the ratio between momentum and thermal diffusion. It is defined as

$$Pr = \frac{\nu}{\kappa}.\tag{2.2}$$

The heat transport in the fluid is characterised by the Nusselt number (Nu), which is defined as the ratio of total heat transfer to conductive heat transfer, i.e.

$$Nu = \frac{qH}{\lambda \Delta T},\tag{2.3}$$

where q is the heat flux density and λ is the thermal conductivity of the fluid. Finally, the geometry of the cell also influences the flow dynamics of the RBC by controlling the impact of the lateral boundaries. This contribution is determined, for a given geometry, by the aspect ratio between the lateral dimension L and the cell height H

$$\Gamma = \frac{L}{H}.\tag{2.4}$$

These control parameters, when combined, allow for the characterisation of RBC and enable the scaling of the flow for both numerical and experimental investigation.

The dimensionless parameters Ra and Pr are a result of a non-dimensionalisation of the governing equations. To obtain this, the velocity is expressed in units of the free-fall velocity (u_f) , defined as

$$u_f = \sqrt{gH\alpha\Delta T} \ . \tag{2.5}$$

This measure represents the hypothetical velocity attained by a fluid parcel travelling a distance H in free-fall conditions, hence under constant acceleration. However, due to viscous dissipation, observed velocities are significantly lower. From the definition of u_f , the corresponding free-fall time (t_f) is derived:

$$t_f = \frac{H}{u_f} = \sqrt{\frac{H}{g\alpha\Delta T}} \ . \tag{2.6}$$

The free-fall time represents a characteristic timescale, reflecting the rapid fraction of the dynamics inherent in the convective flow. To assess the slower dynamics in RBC, the vertical diffusion time is defined for Pr > 1 by $t_{\nu} = H^2/\nu$ and the vertical viscous time for Pr < 1, defined by $t_{\kappa} = H^2/\kappa$. These are compared to determine the effective dissipative time $t_d = max(t_{\nu}, t_{\kappa})$. Another important timescale is the eddy turnover time, which represents the time required for a parcel of fluid to circulate within a convection roll. A more precise definition will be provided later in this chapter.

In turbulent RBC, as in any turbulent system, it is worth assessing as well the Kolmogorov microscales, which represent the smallest flow scales that develop below which viscous dissipation becomes dominant. The Kolmogorov length (η) and time scale (t_{η}) are defined as

$$\eta = \left(\frac{\nu}{\epsilon}\right)^{\frac{1}{4}} \quad \text{and} \quad t_{\eta} = \sqrt{\frac{\nu}{\epsilon}},$$
(2.7)

with ϵ being the average kinetic energy dissipation rate.

In a RBC configuration, when the temperature difference between the plates is sufficiently small, the fluid remains motionless and stable, with heat transport occurring solely through pure conduction. As ΔT and Ra increase, convection will not begin until a critical Rayleigh number (Ra_c) , is reached. For a cell with infinite width $(\Gamma = \infty)$, this value has been analytically demonstrated to be $Ra_c = 1708$ [5, 6]. However, for cells with finite aspect ratio, the critical value is larger and increases as Γ decreases, and further depends on the fluid as well as on the conductivity of the side walls [7, 8]. Above Ra_c , different coherent structures (i.e. structures with lifetime comparable to their transit time through the cell) start to develop. In the regime slightly above the onset of convection, the flow is laminar and takes the form of spatially periodic convection rolls, which are stationary or only slowly evolving in time. These patterns, for $Ra \gtrsim Ra_c$, are susceptible to instabilities and can take the shape of zigzag, eckhaus and oscillatory structures [9] (see Figure 2.1). As Ra increases, new structures, such as plumes and thermals, develop. According to Sakievich et al. [10], plumes are continuous, coherent volumes of hot or cold fluid originating from the boundary layer, transporting heat as sheet or line-like

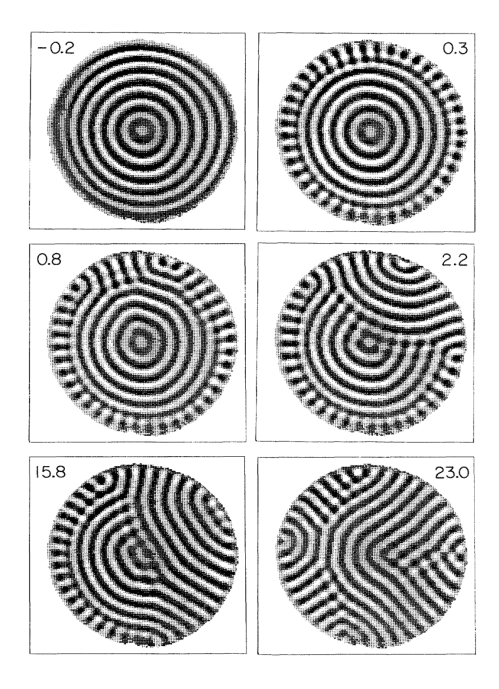


Figure 2.1: Shadowgraph images of the evolution of laminar flow patterns close to Ra_c as a heat flux density change is applied (from Ahlers et al. [4]). The number in each square is the elapsed horizontal diffusion time $(t_h = \Gamma^2 t_\kappa)$. These images, taken from a top view, depict the horizontal temperature distribution, with bright regions indicating cold areas (downflow) and dark regions representing warmer areas (upflow).

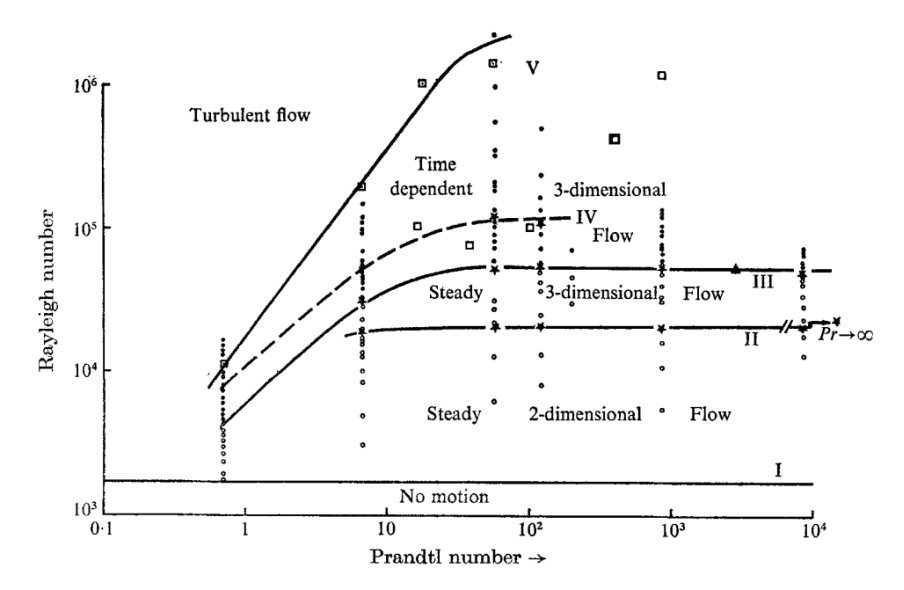


Figure 2.2: Extract of the regime diagram from Krishnamurti [11].

flows whereas thermals are described as detached buoyant blobs rising (or sinking) through the volume. With Ra increasing further, the flow undergoes transitions to non-stationary and turbulent states, entering different regimes dependent on Ra and Pr, as illustrated in Figure 2.2. From a flow dynamics perspective, the behaviour within these regimes has been shown to be strongly dependent on the cell's cross-sectional outline and Γ [8].

For turbulent convection in a container of $\Gamma = 1$, a so called Large Scale Circulation (LSC), exhibiting a single convection roll, develops [12]. Its dynamics are characterised by a variety of modes, ranging from periodic temporal behaviour, such as torsional and sloshing oscillations, to stochastic fluctuations, including spontaneous reorientations and complete flow cessations and restarts [13, 14]. An example of a LSC in a $\Gamma = 1$ cell is shown in Figure 2.3. As described by Kadanoff [15], hot plumes are generated from the flow close to the heating plate and near the left-hand wall of the container. These plumes ascend to the cooling plate and travel along the top surface while cooling. In the same fashion, cold plumes are generated from the flow near the top plate, which descend towards the bottom on the right-hand side of the cell. Upon reaching the heating plate, these cold plumes travel along the bottom, increasing in temperature and entraining newly generated hot plumes, thereby sustaining the circulation indefinitely. The region closest to the heating and cooling plate, in which majority of the temperature drop occurs, and from where the plumes erupt, is termed thermal boundary layer. The region of hot (or cold) plumes moving close to the wall is often referred to as mixing zone or viscous boundary layer. Both boundary layers are not clearly separate, and their dimension with respect to



Figure 2.3: A shadowgraph showing a LSC in a cell with $\Gamma = 1$. From Shang et al. [16].

each other depends on Pr. The central region, termed bulk, contains relatively few plumes in a turbulent motion, which nevertheless contributes to the circulation.

As Γ increases, the coherent convection roll breaks down into more complex and less organised flow structures due to the diminishing interaction with the side walls. This has been observed, for example, at $\Gamma = 1.5$ for cylindrical cells at low Ra [17] or, as Cuba et al. [18] reports, at $\Gamma = 2.5$ for $Ra = 10^7$. Beyond a certain Γ , the flow appears even more chaotic, and well-defined structures can no longer be easily recognised. However, time-averaging the flow field reveals hidden, large-scale structures resembling the convection rolls observed near the onset of convection. These structures are known as Turbulent Superstructures (TSS) and, in highly turbulent thermal convection, are the largest horizontal flow scales that develop, exhibiting flow characteristics, size, and shape that are independent of the system geometry. An example of such structures is shown in Figure 2.4. These structures have been studied and analysed by means of Direct Numerical Simulations (DNS) by Cuba et al. [18], Stevens et al. [19], Pandey et al. [20] and experimentally by Moller et al. [21], Moller et al. [22], Weiss et al. [23] and Ghazijahani et al. [24] through full-field velocity measurements. Besides the characterisation of the topology and the wavelength of the TSS, these studies also quantified the impact of TSS on the heat transport through the characterisation of the local Nu. In particular, Moller et al. [21] concluded that the Nusselt number reaches local maxima coincident with the positions of the TSS, highlighting their significant role in heat transport. Furthermore, methods for determining the optimal averaging time au have been evaluated. The objective is to identify a suitable time window length such that

the fast, small-scale fluctuations of velocity and temperature are separated from the gradual variation of the large scale patterns. This window should be sufficiently long to achieve this goal, but also short enough to avoid obscuring the large-scale patterns themselves.

Pandey et al. [20] proposed a method based on the free-fall time t_f , accounting for the rapid fraction of dynamics of the convection, and effective dissipative time t_d as slower time unit. τ is hence preliminary identified in the range

$$t_f \ll \tau \ll t_d. \tag{2.8}$$

More detailed definitions of this quantity have been investigated by the authors; however, their assessment requires quantities that are not directly measurable in the experiment under study. Weiss et al. [23] investigated the TSS by means of the Shake-The-Box Lagrangian particle tracking velocimetry and employed Proper orthogonal decomposition (POD) to separate the superstructures from the turbulent fluctuations. An analysis of the averaged profiles of horizontal and vertical turbulent kinetic energy (TKE) revealed an estimation of the averaging time of $\tau = 50~t_f$. This value was also confirmed by Ghazijahani et al. [24] through an analysis of the

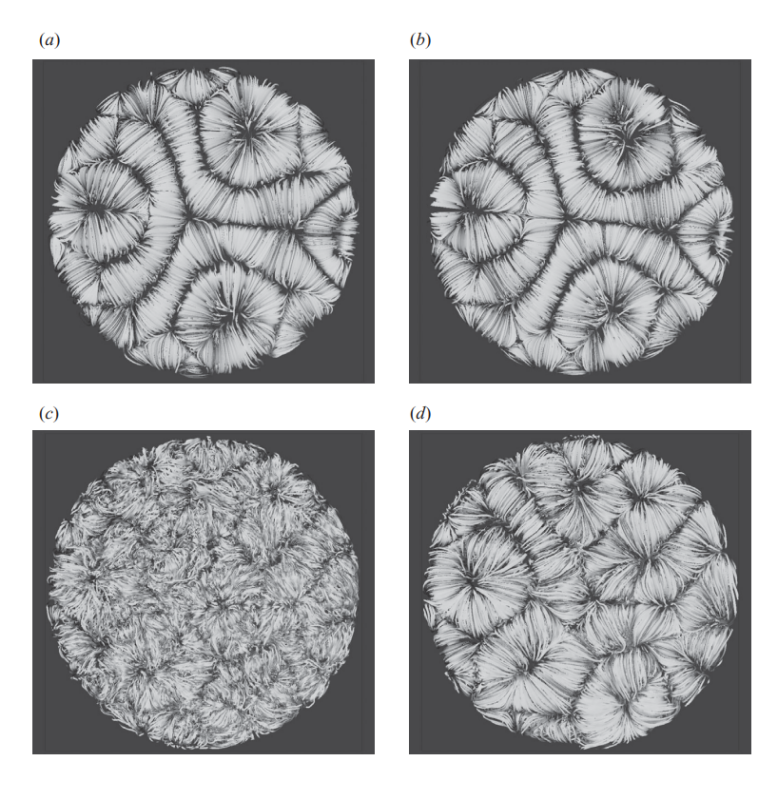


Figure 2.4: Top view of different DNS from Cuba et al. [18] with $Ra = 6 \times 10^3$ (a,b) and $Ra = 10^7$. The streamlines of the instantaneous (a,c) and time-averaged of 50 t_f (b,d) are displayed.

decay of the average temporal cross correlation coefficient, which in their experiment reaches a minimum after $\tau = 57~t_f$.

2.2 Temperature sensitive paint

Surface measurements of pressure and temperature can provide insightful information on flow events such as boundary layer transition, flow separation, shock wave interactions and more complex flow dynamics. To derive the pressure distribution over a model, traditional wind tunnel testing typically employs multiple pressure taps located on the surface, each one connected to a pressure transducer. Piezoelectric or capacitive sensors are also commonly used. Obtaining a comprehensive and detailed pressure field requires a large number of these taps or devices, significantly increasing the complexity and cost of the experiment. However, the resulting pressure field will be limited in spatial resolution due to the discrete placement of the measurements points over the model in study. Temperature fields can be obtained using infrared thermography; however, this technique suffers from drawbacks related to cost and operational complexity, as infrared cameras are typically more expensive than high-speed cameras operating in the visible spectrum. Furthermore, these cameras cannot be positioned external to the wind tunnel without employing windows transparent to infrared radiation. Placing them inside the tunnel, moreover, introduces flow intrusivity and the need of a detailed design of the camera housing tailored to the specific wind tunnel conditions, which is even more critical for tunnels such as the European Transonic Wind Tunnel (ETW) in Köln, which operates at cryogenic temperatures. Additional limitations include reduced spatial resolution and slow acquisition rates.

Pressure-sensitive paint (PSP) and temperature-sensitive paint (TSP) offer an alternative approach as *global measurement techniques*. These techniques provide spatially resolved, non-intrusive, full-field measurements of surface temperature (and pressure, in the case of PSP) over large areas.

2.2.1 Photonics and temperature evaluation

Both PSP and TSP consist of polymer-based paints in which pressure or temperature sensitive luminescent molecules are immobilised [25]. Their working principle relies on the oxygen and thermal quenching of luminescence, as schematically described by the Jablonski energy-level diagram in Figure 2.5. The lowest energy level in the diagram represents the ground state (S_0) of a luminophore molecule, typically a singlet state. Higher energy levels correspond to excited singlet states

 $(S_1 \text{ and } S_2)$ and triplet states (T_1) . Upon absorption of a photon, the luminophore undergoes a transition from a ground electronic state to one of these excited states. The excited electron returns to the ground state by a combination of radiative and radiationless processes. The radiative decay from the lowest excited singlet state S_1 to the ground state is known as fluorescence, while the transition from the triplet state T_1 to the ground state is termed phosphorescence. The latter, being a spinforbidden transition, has a longer lifetime than fluorescence, typically by up to three orders of magnitude. The term luminescence encompasses both fluorescence and phosphorescence. Radiationless deactivation processes are internal conversion (IC), intersystem crossing (ISC) and external conversion (EC), which dissipate energy as heat or transfer it to the surrounding environment. The excited states can be deactivated through interactions with the surrounding environment, with processes such as oxygen quenching and thermal quenching. PSP methods rely on the oxygen quenching process and relate the gas partial pressure above the model surface to the luminescent intensity. TSP methods, instead, are based on thermal quenching, as the paint layer is designed to be impermeable to oxygen. Thermal quenching is associated with temperature: as temperature increases, the quantum efficiency of the luminophore decreases. Quantum efficiency, defined as the proportion of absorbed energy re-emitted as light, is inversely proportional to the temperature; a higher temperature leads to a higher frequency of collisions between particles and, consequently, an enhanced probability of deactivation via external conversion.

To obtain a relation between luminescent intensity and temperature, a simplified model of the luminescence is assessed, considering only the main processes: excitation, luminescence radiation, non-radiative deactivation and quenching. The detailed model derivation is provided in Liu et al. [25]. For TSP experiments conducted within a limited temperature range, the relation between intensity and temperature is obtained by fitting a curve of the Arrhenius type:

$$\ln \frac{I(T)}{I(T_0)} = \frac{E_{nr}}{R} \left(\frac{1}{T} - \frac{1}{T_0} \right), \tag{2.9}$$

where T is the temperature, I(T) is the luminescent intensity at temperature T, T_0 is the reference temperature, $I(T_0)$ is the intensity at the reference temperature, E_{nr} is the activation energy for non-radiative processes and R the universal gas constant. In case the experimental data do not fully obey the Arrhenius relation, an alternative empirical functional relation may be employed:

$$\frac{I(T)}{I(T_0)} = f\left(\frac{T}{T_0}\right),\tag{2.10}$$

Vibrational Internal **Triplet Excited** Conversion Relaxation State Interstystem Crossing T_1 Internal Energy Adsorption Fluorescence and Phosphorescence External Conversion Ground Vibrational

Singlet Excited States

Figure 2.5: The Jablonsky energy-level diagram (from Liu et al. [25]).

Relaxation

where $f\left(\frac{T}{T_0}\right)$ can be a polynomial, exponential or other function chosen to best fit the experimental data within the observed temperature range.

2.2.2 Typical TSP experimental setup

Commonly employed TSPs in experimental studies are tris(2,20'-bipyridyl) ruthenium (Ru(npy)) complexes dispersed in automotive clear coat, or europium(III) thenoyltrifluoroacetonate (EuTTA) complexes in model airplane dope. The luminophores can be excited by UV light, nitrogen lasers, frequency-tripled YAG lasers or blue LED arrays, depending on the complex employed. Luminescent molecules, serving as sensors, are incorporated into a polymeric coating. This coating is typically prepared by dissolving the luminophore and polymer binder in a solvent, then applied to the surface using a sprayer or airbrush.

Ideally, TSPs should exhibit high luminescent output to maximise the signal-to-noise ratio (SNR), which is also influenced by the paint layer thickness. A stable luminescent output under continuous excitation is also desirable, although in reality it is often limited by photodegradation. In addition, TSPs require sufficient temperature response time and appropriate sensitivity for the intended application range. Finally, the polymer binder should possess physical characteristics - such as adhesion, hardness, smoothness, impermeability, and controlled thickness - selected

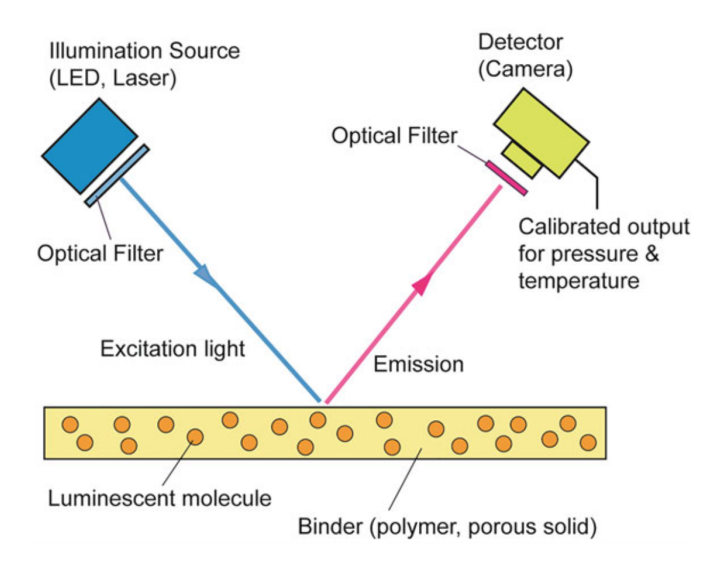


Figure 2.6: Schematic of the component of a PSP/TSP experiment (From Liu et al. [25]).

based on the specific experimental requirements.

Measurement systems for TSP fall into two main categories: intensity-based methods and lifetime methods. Regarding intensity-based methods, camera systems are the most common acquisition setup. A typical measurement system, illustrated in Figure 2.6, employs an illumination source (UV lamp, LED array or laser) to excite the TSP. Optical filters are used to avoid projection of the excitation light onto the camera sensor and to minimise the capture of stray illumination. In intensity-based methods, images of the TSP are acquired both in wind-off (wind tunnel inactive) and wind-on configuration, and then transferred to the data system. To characterise the noise of the camera sensor, a dark current image is acquired with shutter closed or with the lens cap on. In addition, a dark image is also captured in the absence of illumination from the source, to account for possible unwanted light sources in the wind tunnel or laboratory. These two images are subtracted from all the frames captured during the experiment. A ratio between the wind-on and wind-off images is then calculated, obtaining a luminescent intensity ratio image. For each pixel, the calibration curve associated with the paint is used to extract the distribution of surface temperature.

In lifetime-based methods, the paint intensity decay time following an illumination pulse or wave is related to the pressure or the temperature at the surface. A detailed discussion of this method falls outside the scope of this thesis, as it was not employed during the experimental campaign.

Chapter 3

Experimental setup

3.1 Rayleigh-Bénard experiment

An existing Rayleigh-Bénard convection facility was used to investigate the turbulent superstructures in RBC. It was designed with the flexibility to vary the cell aspect ratio Γ and temperature difference ΔT and guarantee optical access from its top while maintaining thermal insulation. It has been formerly employed by the studies performed by Weiss et al. [23], who investigated RBC through Langrangian particle tracking velocimetry. A schematic illustration of the system is presented in Figure 3.1. The fluid volume has a quadratic outline of $W \times L = 320 \times 320 \text{ mm}^2$.

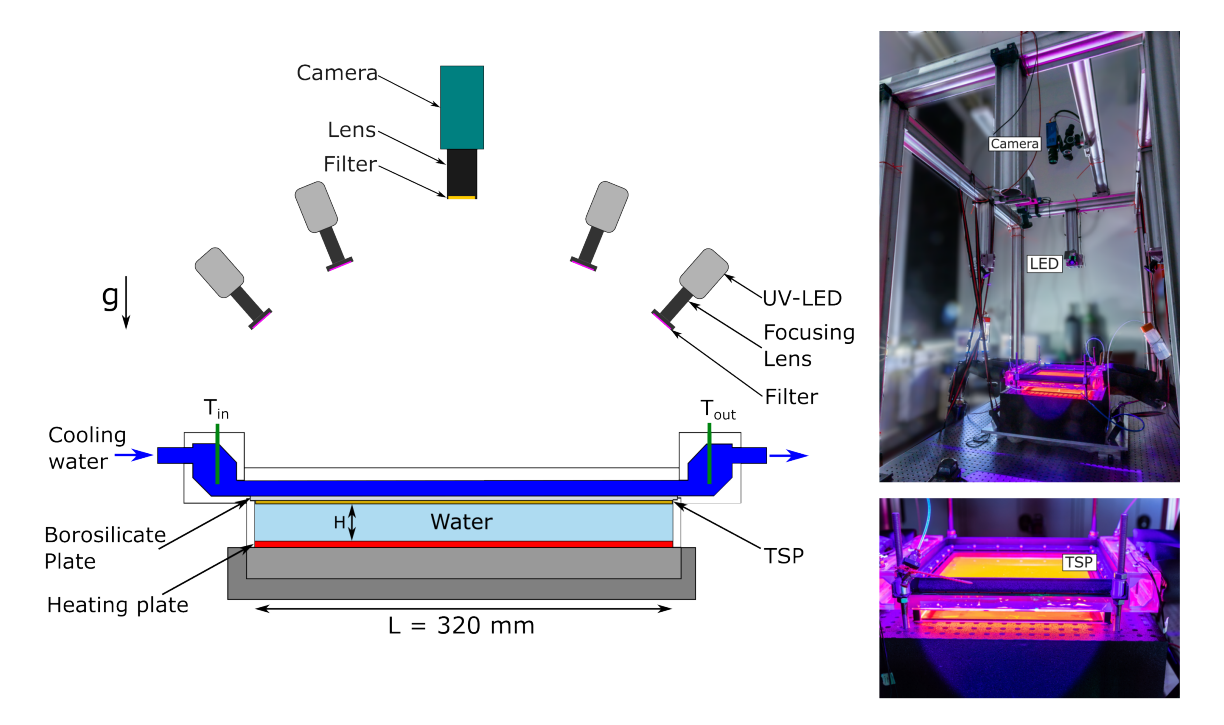


Figure 3.1: Schematic overview of the setup and images of the cell illuminated by UV light (photo credit: J. Agocs).

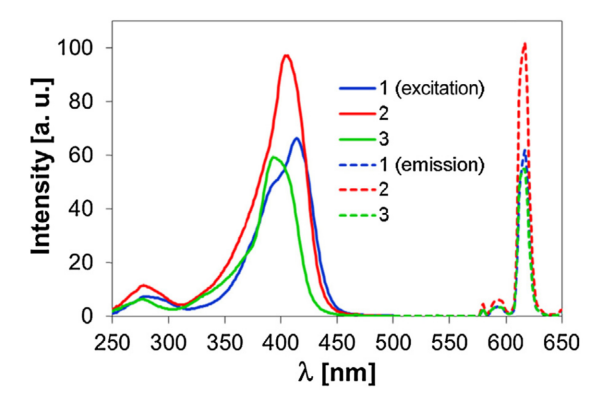


Figure 3.2: Excitation and emission spectra of three different Europium complexes (From Ondrus et al. [26]). Number 1 has been employed in the present study.

The bottom plate is an aluminium plate with a thickness of 30 mm. It is heated via a carbon fibre fabric glued to its bottom. Thermal insulation is provided below and beneath the plate by a 18-cm thick polypropylene foam, which ensures a homogeneous temperature distribution over the heated surface. Four resistance temperature detectors (Pt1000, 1/3 DIN B) are embedded 5 mm below the upper surface and placed at the centre of each quadrant. The thermistors' measured temperatures are used as input for a PID control loop that maintains a constant average plate temperature T_b within an accuracy of ± 5 mK. The cell's side walls, with a thickness of 12 mm, are made of plexiglass and define the height H of the fluid sample. Four different sidewalls, varying in H, were manufactured, with heights of 10, 20, 40 and 80 mm, corresponding to $\Gamma = 32$, 16, 8, 4, respectively.

A transparent borosilicate top plate of thickness 1.1 mm is placed on top and sealed with silicon to the side walls. In order to ensure both cooling of the top plate and optical access to the TSP, water is employed as cooling fluid and is circulated at a defined temperature through a cavity above the top. The cooling water temperature, which defines, with minor adjustments, the top plate temperature T_t , is regulated by a chiller and kept constant within ± 10 mK. Two thermistors are submerged in the cooling flow prior to the passage over the cell, and two are placed at the outlet. Distilled water serves as the working fluid in both the convection cell and the cooling circuit.

The top plate is coated on the lower side with a layer of temperature sensitive paint (TSP) based on a Europium complex (Europium 1,3-di(thienyl)propane-1,3-diones), embedded within a polyurethane (PUR) matrix [26]. Excitation and emission spectra of the TSP are illustrated in Figure 3.2. The thickness of the TSP layer was measured with a profilometer and determined to be $40 \pm 0.1~\mu m$ for measurements $\Gamma = 32$ and $\Gamma = 16$, and to $20 \pm 0.1~\mu m$ for measurements with $\Gamma = 8$ and

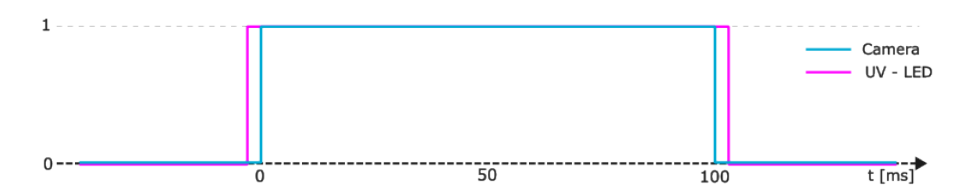


Figure 3.3: Schematic representation of the trigger timing.

 $\Gamma=4$. The TSP layer is in direct contact with the working fluid. The dye is excited using four LEDs arranged in a square configuration above the convection cell. The LED housing employed is a proprietary design of the Department of Experimental Methods of the Institute of Aerodynamics and Flow Technology in DLR Göttingen and is built around the chip Luminus SBM-120-UV-395nm, powered through a dedicated power supply. Each LED housing is equipped with a cooling fan to ensure thermal stability of the chip throughout each run. The light emitted from the chip is directed towards the TSP by means of UV focusing lenses (HSO-PL-720-UV). Filters (Chroma ET385/70X) are attached to the lenses to restrict the light spectrum to the UV wavelengths (350-420 nm). To capture the TSP emission, a CCD camera (PCO PCO.4000) is placed centrally and perpendicularly with respect to the cooling plate 2 meters above the setup and equipped with a 35mm lens (Carl Zeiss Distagon T* 2.8/35). A filter (Chroma ET630/75m) is mounted to the camera lens to isolate the TSP emission spectrum (592-668 nm) and minimise stray light interference.

3.2 Experimental procedure

Prior to each experimental run, the bottom and top plates were set to their target temperatures to achieve the desired ΔT . The cell mean temperature was selected to be approximately 20 °C to maintain Pr=7 and ensure comparability between different cases, other experiments and DNS results. Furthermore, this temperature, being close to ambient laboratory conditions, minimised heat flux through the side walls. After reaching the desired temperature, a stabilisation period of at least 30 minutes (500 to 2500 t_f) was provided to allow the flow to adapt to the thermal boundary conditions and ensure fully developed thermal structures. To maximise optical power output while limiting thermal stress on the UV-chip, the LEDs were operated in pulsed mode. Their duty cycle was calibrated to initiate the illumination window 3 ms before the camera exposure trigger, as illustrated schematically in Figure 3.3. This timing, determined through oscilloscope analyses, aimed to cut

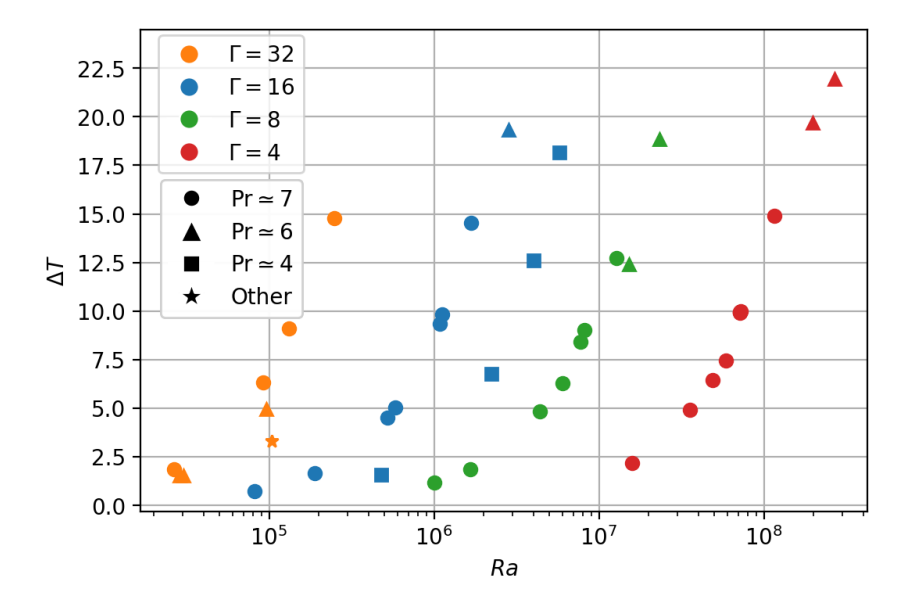


Figure 3.4: Overview of the measurement points acquired.

the first transient increases in LED light intensity upon pulse initiation. During the measurement campaign, the cooling fans were always activated and, prior to each acquisition, the LEDs were pulsed for a minimum of 5 minutes to ensure thermal equilibrium and stable illumination. The camera exposure time and pulse repetition frequency of both the LEDs and camera system were selected based on the characteristic flow velocities. Before each measurement campaign, and therefore for each Γ , a "camera dark current" image was captured to account for data transfer noise. Each experimental run lasted approximately 50 minutes, recording from 1000 to 7000 t_f depending on Ra, with plate temperatures continuously monitored to ensure stability.

The measured points acquired are displayed in Figure 3.4,

3.3 Uncertainty analysis and measurement accuracy

The typical application of TSP is in experiments with measurement times on the order of milliseconds or seconds, to fully exploit the paint's fast response time. Furthermore, during conventional measurement campaigns, the properties of the setup components (LEDs and paint) are assumed to remain constant. The application of a TSP setup to a slowly-evolving flow like the Rayleig-Bénard convection, with the TSP submerged in water for extended periods and the LED operated with high-power pulses for prolonged durations, represents an innovation in experimental fluid

dynamics [25]. This presents several novel challenges that were addressed during the course of this study through dedicated experiments and testing.

The following sections present in detail the considerations made regarding these aspects as well as assessment of the measurement accuracy.

3.3.1 Temporal and spatial resolution

While in most TSP experiments, the camera is positioned to image the face of the TSP coating which is in contact with the flow, in the current experiment, instead, the camera acquires images of the TSP surface opposite to the flow, hence of its "cold" side. An assessment of the rate at which information is transmitted through the paint layer is hence required. This was studied by analysing the response time of the TSP to the temperature fluctuations in the working fluid, which was estimated employing the diffusion time $t_{\rm diff}$, defined as

$$t_{\text{diff}} = \frac{\delta_{\text{TSP}}^2}{\kappa_{\text{PJUR}}},\tag{3.1}$$

where δ_{TSP} is the thickness of the TSP layer and κ_{PUR} the thermal diffusivity of the polymer matrix. For polyurethane, a value from the literature was employed: $\kappa_{\text{PUR}} \approx 5 \times 10^{-7} \frac{m^2}{s}$ [27]. For a TSP thickness $\delta_{\text{TSP}} = 20~\mu\text{m}$, it results $t_{\text{diff}} \approx 0.8~\text{ms}$, and for $\delta_{\text{TSP}} = 20~\mu\text{m}$, $t_{\text{diff}} \approx 3.2~\text{ms}$. Their values, when compared with the Kolmogorov time scale t_{η} , which ranges from 0.7 to 1.7 s across the experiments employed during the evaluation (See Table A.1), confirms that the delay of the temperature signal transmission through the TSP can be considered negligible. The camera exposure time t_{exp} was set such that it would result

$$t_{\text{diff}} \ll t_{\text{exp}} \ll t_{\eta},$$
 (3.2)

to ensure sufficient signal in the acquired images without losing temporal information. To allow time-resolved measurements, the recording frame rate was selected to be higher than t_{η} . However, its value was intentionally chosen to be of a similar order of magnitude, acknowledging that a higher value would not yield large improvements in resolving the fastest temperature fluctuations. As a result, the number of images captured per Kolmogorov time scale, is $\frac{img}{t_{\eta}} > 1$ for all measurements (with the exception of measurement #3 in Table A.1).

The spatial resolution of the measurement was assessed using the determined scale factor of $3.6 \pm 0.03 \frac{px}{mm}$. Comparing this value with the Kolmogorov length η , which ranged from 0.8 to 1.3 mm across the measurements, yields a resolution

ranging from 2.5 to 4.7 $\frac{\text{px}}{\eta}$.

These estimations demonstrate that the current experimental setup is capable of obtaining spatially and temporally resolved measurements.

3.3.2 Assessment of temperatures

To calculate Ra as well as Pr and to process the images, a precise determination of the thermal boundary conditions of the RBC cell was required. This was achieved by utilising the data from the four thermistors positioned on the bottom plate, the four on the cooling flow inlet and outlet, and the bottom plate power supply.

The heat flux density was calculated as

$$q = \frac{\dot{Q}}{A},\tag{3.3}$$

where \dot{Q} represents the mean power supplied to the bottom plate measured by the power supply and A the cross sectional area of the cell.

The mean bottom and top plate temperatures were calculated for each measurement case as

$$T_b = \langle T_{b_{th}} \rangle - q \frac{\delta_{alu}}{\lambda_{alu}} \quad and \quad T_t = \langle T_{t_{th}} \rangle + q \frac{\delta_{boro}}{\lambda_{boro}},$$
 (3.4)

where $\langle T_{b_{th}} \rangle$ and $\langle T_{t_{th}} \rangle$ represent the mean of the temperature measured by the four thermistors on the bottom and top plate respectively, $\delta_{alu}=5$ mm the distance between the thermistors on the bottom plate and the fluid, and $\delta_{boro}=1.1$ mm the thickness of the borosilicate glass plate. $\lambda_{alu}=200~\frac{\rm W}{\rm m\cdot K}$ and $\lambda_{boro}=1.2~\frac{\rm W}{\rm m\cdot K}$ are the thermal conductivities of the aluminium plate and borosilicate glass plate, respectively. During the calculation it has been assumed

$$\frac{\delta_{\text{TSP}}}{\lambda_{\text{TSP}}} \ll \frac{\delta_{boro}}{\lambda_{boro}},$$
 (3.5)

given the different orders of magnitude in thickness between the TSP layer and the borosilicate plate and given the difficulty in accurately measuring λ_{TSP} . However, to ensure a conservative estimate during the analysis, the contribution of the TSP to the temperature correction was accounted for by increasing δ_{boro} by 0.1 mm.

The temperature difference ΔT and the cell mean temperature T_m were then calculated using

$$\Delta T = T_b - T_t \quad and \quad T_m = \frac{T_b + T_t}{2}.$$
 (3.6)

3.3.3 Rayleigh number

To extract accurate values of Ra and Pr, the C++ library CoolProp [28] was employed. For water, the library utilises the IAPWS-95 equation of state (EOS), a thermodynamic model developed by the International Association for the Properties of Water and Steam (IAPWS) [29]. Using as input T_m , ambient pressure $P_{amb} = 99536$ Pa (extracted employing the 1976 Standard atmosphere model [30] at Göttingen's elevation) and gravitational acceleration $g = 9.80665 \, \frac{\text{m}}{\text{s}^2}$, the library calculates ρ , α , the thermal conductivity λ_w , and the heat capacity C_p . These values were then used to compute the thermal diffusivity $\kappa = \frac{\lambda_w}{\rho C_p}$. Subsequently, Ra and Pr were calculated using Equations 2.1 and 2.2.

3.3.4 Nusselt number

An estimation of the Nusselt number Nu was performed to assess the optimality of the boundary conditions by comparison with DNS results and other experiments.

To identify a suitable Nu power law for reference, different sources were examined, as most of the empirical correlations obtained over the years to deduce Nu = f(Ra, Pr) suffer from range limitations and discrepancies with experimental results, making a universally applicable law difficult to define. Grossmann et al. [31], and subsequent updates [32], proposed a unifying theory to account for both Nu = f(Ra, Pr) and Re = f(Ra, Pr), based on a large collection of experimental data. This model is widely employed in the scientific community due to its complete-

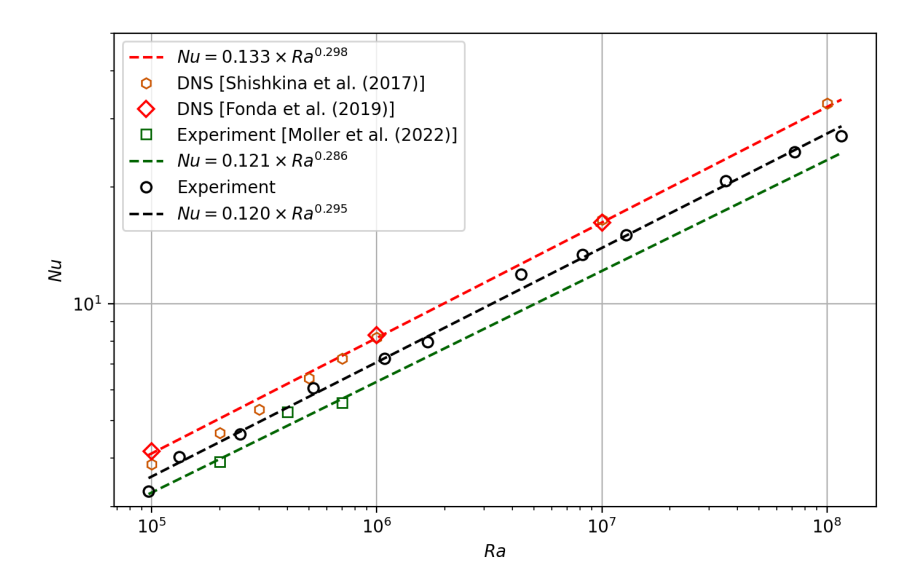


Figure 3.5: Nu as function of Ra from the experiment in study (black circles) and from previous experiment (green squares) and DNS (orange hexagons, red diamonds) by others.

ness and versatility; however, the theory is mostly valid for volumes with $\Gamma = 1$, and insufficient experimental data exist to define a power law in the relevant Ra region for the current experiment. Therefore, a different law is required. Fonda et al. [33] conducted DNS on a domain with $\Gamma = 25$ at Pr = 7 and $Ra = 10^5, 10^6$ and 10^7 , which represent a more relevant range for this study. Curve fitting to the Nu values obtained from these simulations yields the relationship $Nu = 0.133 \times Ra^{0.298}$. This fit is also consistent with the Nu obtained by Shishkina et al. [34], who conducted DNS at different Ra at Pr = 5 in a cylindrical container with $\Gamma = 1$. These numerical simulations employed perfectly isothermal bottom and top plates, and represents a result to which the experiment can be compared when assessing boundary condition optimality. Moller et al. [22] employed an apparatus similar to the one used here for their investigations on RBC, and extracted the fit $Nu = 0.121 \times Ra^{0.286}$. The Nu calculated from the data relevant for the current study (Table A.1) are plotted as black circles in Fig. 3.5. They are rather close to experimental measurements and results from DNS and, in particular, show the same slope in the log-log plot. In fact, a power law fit to the data results in $Nu = 0.120 \times Ra^{0.295}$.

As can be observed from the figure, both experimental measurements find lower Nu compared to the DNS. It has to be noted that neither experiments are ideally suited for high precision heat flux measurement: Moller et al. [22] calculated it from averaging temperature and velocity data obtained via particle tracking, potentially leading to an underestimation, while in this experiment the \dot{Q} provided by the power supply was used, thereby neglecting the losses in the cabling and the bottom plate, and hence leading to an overestimation. However, for the purpose of boundary condition assessment, these results can still bring valuable information.

The lower Nu measured can be attributed to non-ideal boundary conditions at the sidewalls or at the top plate. However, given the high Γ at which the experiments were performed, and given that T_m was selected to mitigate the contribution from the sidewalls, the heat flux from them can be considered negligible. The non-ideality of the boundary conditions at the top plate, instead, could play a higher role, as its design for both experiments prioritised optical access over thermal insulation. Due to its finite thermal conductivity, a temperature drop occurs across the height of top plate that depends on the local heat flux in the fluid right below (see also Eq. 3.4). It is the spatial heat flux variation together with the finite conductivity of the top plate that leads to the development of spatially varying temperature on the bottom side of the top plate, which we measure using TSP. A more detailed analysis considering the Biot number could better quantify these effects.

3.3.5 Biot number

From the estimation of Nu, it is possible to assess the Biot Number (Bi) which relates the thermal resistance due to thermal conduction within the plates and the convective heat transfer at the plates. It is used as a figure of merit for the uniformity of the boundary conditions in the experiment. Given the similarities in the setup, Bi is calculated with the formulation employed by Moller et al. [22]. As in their work, two Bi are relevant for understanding the boundary conditions optimality: the Bi of the top plate and the Bi of the bottom plate. They are defined by

$$Bi_t = Nu \frac{\lambda_w}{H} \frac{\delta_{boro}}{\lambda_{boro}} \quad and \quad Bi_b = Nu \frac{\lambda_w}{H} \frac{\delta_{alu}}{\lambda_{alu}}.$$
 (3.7)

For the current setup, the Biot numbers were found to be ranging for Bi_b from 0.023 to 0.046, and for Bi_t from 0.14 to 0.2. Since isothermal conditions can be reasonably assumed for $Bi \ll 1$, this criterion is well satisfied for the bottom plate and is also met for the top plate, albeit to a lesser extent. Moller et al. [22], employing a much thicker glass plate (8 mm), reported a Bi_t ranging from 0.86 to 1.22. This result, indicating less ideal boundary conditions, is consistent with the conclusions presented in Figure 3.5. However, as Weiss et al. [23] state, limited research is available regarding the influence of non-ideal boundary conditions on the flow structures. Vieweg et al. [35] conducted a comparative study using a digital twin of the experimental configuration of Moller et al. [22], systematically relaxing the assumption of ideal thermal boundary conditions. Their simulations showed that the characteristic horizontal size of the long-lived large-scale flow structures, such as the TSS, increases as the boundary conditions become less idealised. This increase is due to the finite thermal diffusivity of the glass top plate, which develops horizontal thermal inhomogeneities. Given the similarities between the present experimental setup and the of the one simulated in a digital twin, a comparable, albeit less pronounced, effect is anticipated.

3.3.6 Richardson number

In order to elaborate on the efficiency of the cooling flow above the top plate, the Richardson Number (Ri), which expresses the ratio of natural convection to forced convection, has been estimated. It is defined as

$$Ri = \frac{g\alpha(T_s - T_\infty)L}{V^2},\tag{3.8}$$

where L is the length of the cooling plate in flow direction and V the flow velocity. T_{∞} represents the temperature of the water before flowing over the cell and it was determined by averaging the temperatures measured by the two thermistors positioned at the cooling plate inlet. T_s represents the temperature of the top plate surface in contact with the cooling flow. As direct measurement of this value was not feasible, and acknowledging that $\langle T_{th} \rangle < T_s < T_t$, it was approximated using:

$$T_s = \frac{\langle T_{t_{th}} \rangle + T_t}{2}. (3.9)$$

In the analysed runs, Ri ranged from 0.05 to 0.3. As natural convection is typically negligible when $Ri \lesssim 0.3$ [36], it can be concluded that forced convection dominates the cooling flow, effectively removing heat imprinted on the top plate by the thermal structures. However, due to uncertainty in the term $(T_s - T_\infty)$, this analysis remains an approximation, providing just an upper bound for the value of Ri.

3.3.7 Stability of TSP in water

Limited experience exists in the literature regarding the application of TSP in water for extended periods, and few studies have investigated the behaviour of TSP when submerged [38]. Lemarechal et al. [37] conducted studies on the evolution of TSP emission in water using the same Europium based paint in polyurethane (PUR) matrix as employed in the current study. As shown in Figure 3.6, the TSP emission (I) shows, in the first 24 h, a steep decay upon submersion, compared to the sample exposed to air. The rate of decay appears to significantly reduce between approxi-

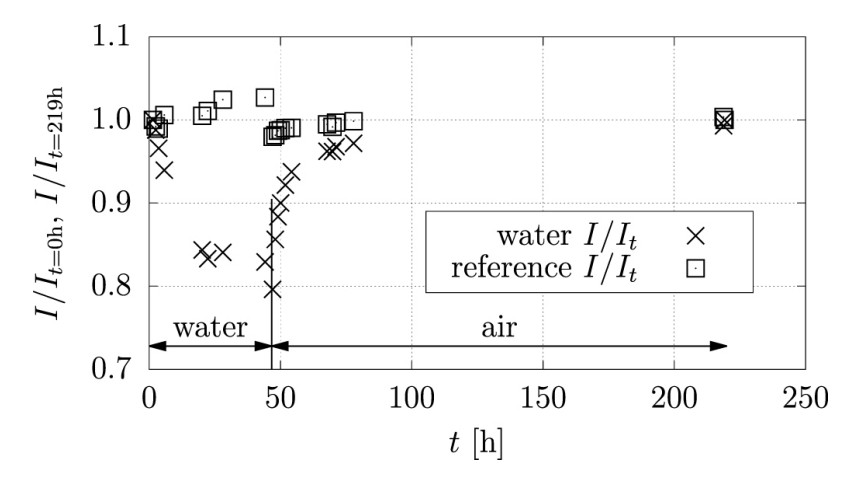
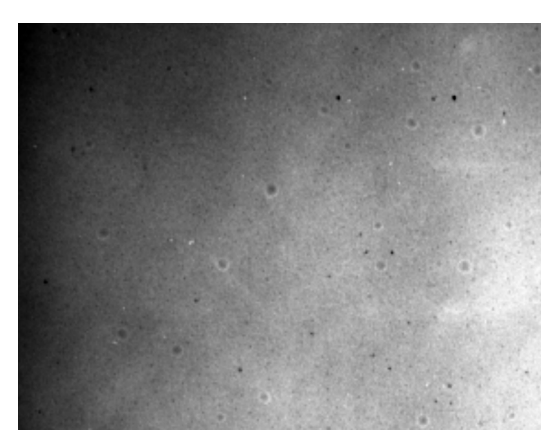


Figure 3.6: Emission of a TSP sample submerged in water (\times marker) compared to a reference sample in air (\square marker). The sample in water exhibits a gradual emission decay over $t \approx 49$ h, followed by a recovery upon drying. From Lemarechal et al. [37].

mately 25 h to 50 h, and the reduction saturates at 15%. The TSP sample was then removed from the water at $t \approx 49$ h and let dry. The emission recovered its original value after approximately 175 h. Analyses conducted on the TSP spectrum by a spectrofluometer concluded that the TSP luminophores are not affected by exposure to water. Instead, the observed intensity decay is attributed to water diffusing into the PUR matrix, altering its optical properties. These changes involve a significant reduction in transmittance at wavelengths necessary for TSP excitation and reduced transmission of approximately 30% in wavelengths relevant to the phosphorescent signal.

However, the results of this study were not directly applicable to the present experimental conditions. A first problem arose from the RBC cell assembly, which comprised filling the system with water (thereby exposing the TSP to the fluid), sealing the cell and cooling circuit, and degassing of the entire apparatus. This process required several hours (≈ 24 h) to be completed, as the water must be connected between the cell and cooling system to ensure fast pressure equilibration between the convection cell and the cooling water, in order to prevent damage of the borosilicate top plate. Due to the complexity of the setup, allowing the TSP to dry between measurements was impractical. As each measurement campaign for a given Γ lasted approximately one week, degradation of the mechanical properties of the TSP was observed.

Figure 3.7a shows a close-up of a TSP image after 8 days of submersion in water, revealing the development of circular imperfections, which are bubbles of water inclusions within the paint. Their number and dimensions depend on the TSP thickness



(a) TSP degradation in forms of "bubbles" after 8 days of submersion in water, as seen in one of the raw images.



(b) TSP degradation after 1 month of submersion and recent drying.

Figure 3.7

and the time of submersion. These imperfections alter the TSP signal transmitted to the camera, creating a lens-like effect. However, given the high resolution of the images, these effects are almost negligible during the initial measurement days, but become much more visible with prolonged experimentation. An example of TSP degradation after one month of submersion in water and subsequent drying is visible in Figure 3.7b, although no measurements were taken with TSP samples submerged for longer than two weeks.

3.3.8 Transient intensity evolution

The spatially averaged luminescent intensity of the TSP layer during the measurement runs reveals a characteristic temporal drift. As shown in Figure 3.8a, the TSP emission intensity varied over time during an experimental run, deviating from the expected constant behaviour. Instead, the intensity changed non-monotonically over one hour, initially increasing to a maximum before decreasing approximately linearly. These variations of almost 2% (although occasionally larger in other measurements), compared to the TSP sensitivity of approximately 4 %/K in this range of temperatures [26], result in a temperature uncertainty of more than 0.5 °C. A correction is therefore necessary.

To better understand this process and isolate the contributing factors, a reference material was introduced to measure the change of the illumination intensity, as the temperature of the LED chip and housing is known to influence light output,

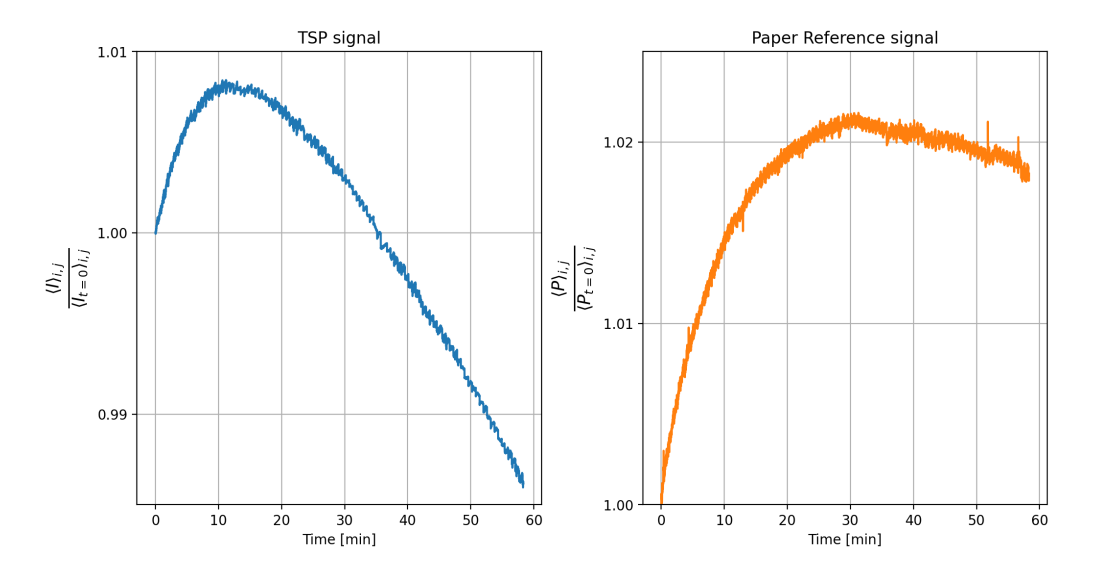


Figure 3.8: TSP and reference intensity temporal evolution throughout a run ($\Gamma = 8 \Delta T = 20K$). The measurement was taken with LED pulsed at 2 Hz and duty cycle of 20%. The values are normalised for the intensity of the frame at t = 0 min.

typically decreasing with increasing temperature. Paper was selected as a "temperature insensitive" reference material by placing two strips alongside the RBC setup to monitor the LED light intensity.

The reference intensity data gathered was spatially averaged to obtain a single value per frame. The temporal evolution portrayed in Figure 3.8b reveals an output variation of 2% over one hour. These data show which part of the variations in the TSP emission origins from variations in the LED intensity and how much is related from changes of the TSP. The TSP intensity was then normalized by the reference signal, as shown in Figure 3.9. As can be seen, the effect of the light source output variation, which was influencing the initial part of the curve in 3.8a with an increase of 0.8%, has been accounted for and compensated. However, a linear decay of 3 %/h remains. A separate set of experiments was performed to further investigate this effect.

First, the wavelength spectra of paper emission and LED chip output were investigated. The data-sheet of the LED chip shows that the spectrum of the emission has a sharp peak centred with respect to the wavelength range of the UV filter. The data-sheet also provides the wavelength peak shift with respect to chip temperature, which is small ($\approx 0.04 \, \frac{\rm nm}{\rm \circ C}$) and remains within the filter range. The luminescence spectra of the paper was instead measured in a TSP calibration facility. The paper sample was excited with constant power and different UV wavelengths corresponding to those transmitted by the UV filters, and the resulting emission spectrum was analysed using a spectrometer. The results indicated that the luminescence inten-

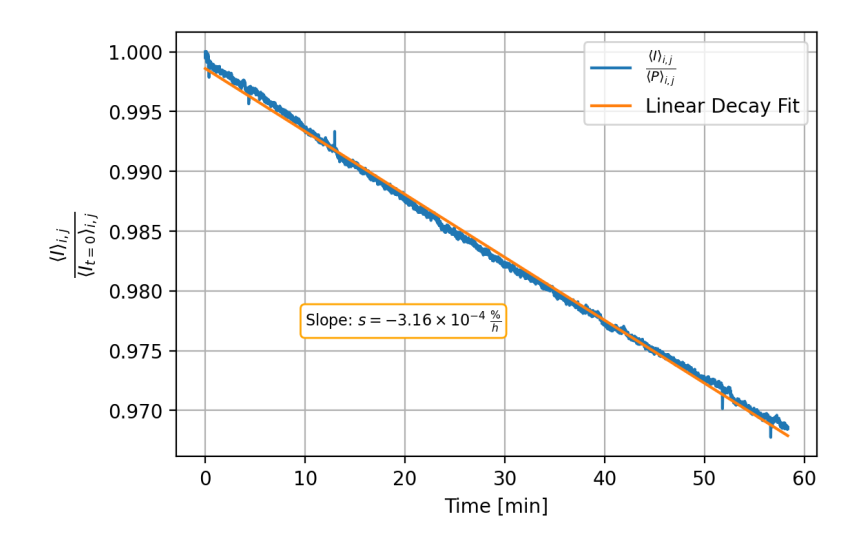


Figure 3.9: Normalised TSP emission intensity for constant temperature as function of time. Normalisation was done by dividing the signal with the reference signal from the paper strips as well as by the initial intensity at t=0 min.

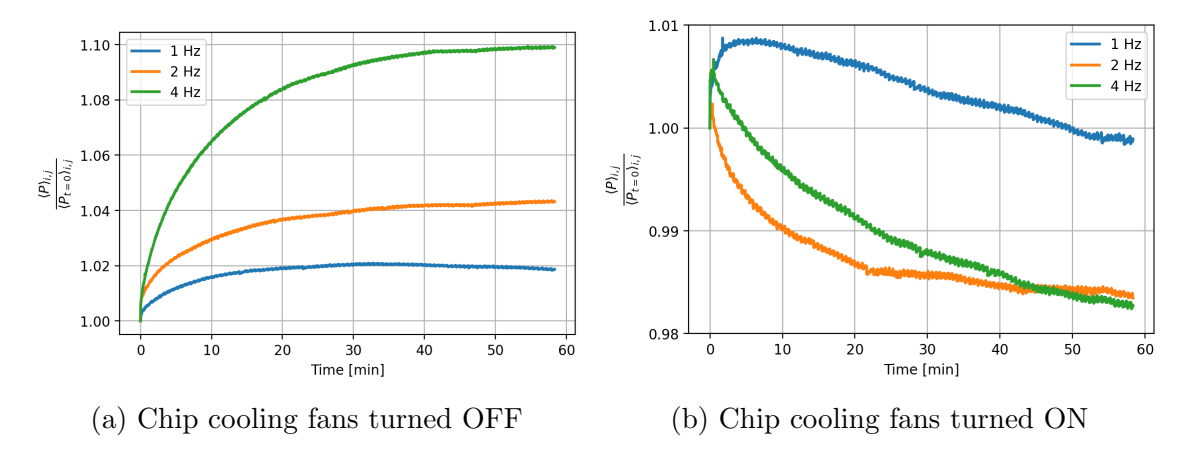


Figure 3.10: Measurement of the spatially averaged intensity of a paper sample $(\langle P \rangle_{i,j})$ excited with UV light at pulse frequencies $f_{rep} = 1, 2, 4$ Hz at duty cycle 10, 20 and 40%, respectively. The values are normalised for the intensity of the frame at t = 0 min.

sity remained stable across the tested wavelengths, and the wavelength peak shift remained within the camera filter range. These findings confirm that variations in the paper luminescence only reflect changes in LED intensity, and is not caused by a shift of the LED spectrum in combination with the spectral filter in front of each LED.

Further investigations were undertaken using the same LED configuration of the RBC experiments, with the paper sample positioned directly above the experimental cell. The sample was illuminated with UV light emitted from the LEDs at different pulse frequencies ($f_{rep} = 1, 2, 4$ Hz at duty cycle 10, 20 and 40%, respectively, corresponding to the RBC cases) for a duration of one hour. The image acquisition was started simultaneously with the initiation of the LED illumination pulses. Firstly, three runs were performed with the LED chip cooling fan deactivated. As illustrated in Figure 3.10a, the intensity of the LED showed a first rapid increase within the first 10-20 minutes. The amplitude of this increase was dependent on the pulse repetition frequency, reaching approximately 10% for the case with 4 Hz. The intensity trend, resembling the one of a saturating exponential, approaches then an asymptotic value, albeit with a slight continued increase. This result contrasts with the LED chip data-sheet, which reports an intensity decay of approximately 3% for a temperature increase of $10 \,^{\circ}C$. A plausible explanation for this behaviour is heating of the LED case rather than the chip itself. The same tests were then repeated with the chip cooling fans activated. The results, displayed in Figure 3.10b, showed that the intensity, following an initial short increase, decreased, approaching an asymptotic value. The magnitude of this variation, however, was limited ($\approx 2\%$) compared to the one observed with the fans deactivated ($\approx 2\% \sim 10\%$). This trend more closely resembles that reported in the LED chip data-sheet, suggesting that the cooling fans effectively dissipate heat from the LED case, while the effect of chip heating remains. These tests demonstrated that the LED cooling fans can ensure a more stable output, but a correction with a reference signal still remains necessary.

Having accounted for the contribution of the LED output, the observed linear decay in the normalised intensity evolution displayed in Figure 3.9 is possibly attributable to effects inherent to the TSP itself. These include the luminescence decrease due to submersion in water, as analysed in Section 3.3.7, or photodegradation of the luminophore following illumination by the high-power UV-LEDs.

Chapter 4

Data processing

4.1 Temperature Calibration

4.1.1 General Remarks

The calibration process allows to relate the information of TSP luminescence to physically meaningful temperature fields. For the experiment in this study, two types of calibration can be employed. The first calibration method allows to relate the TSP luminescent intensity to absolute temperatures. The second, employed here, provides temperature fluctuations with respect to a reference. Hereto, conventional wind tunnel TSP measurements using intensity-based methods (Section 2.2) usually follow a two-step procedure. A reference image is first acquired with the wind tunnel inactive ("wind-off" image). Subsequently, a series of images is captured while the wind tunnel is operating ("wind-on"). The ratio between the wind-on and wind-off images is then used with a calibration formula (Eq. 2.9 or Eq. 2.10) to determine the temperature difference relative to the wind-off condition. To replicate the windoff and wind-on procedures in the present experiment, the initial step is to establish thermal equilibrium within the cell (hence having $T_b \simeq T_t$) and acquire the reference image. Afterwards, a ΔT would be applied, while maintaining T_t constant. However, this approach presents different practical problematics. An issue is that, as the bottom plate does not have any means for cooling, the time required for the entire fluid volume to reach thermal equilibrium, and thus having T_t at the bottom plate, is dependent only on the thermal diffusivity of water, which is low ($\simeq 0.143 \frac{\text{mm}^2}{\text{s}}$ [39]). This results in extended waiting times, up to several hours for the fluid volume with $\Gamma = 4$. These waiting times are not acceptable due to the luminescent decay of the TSP, which diminishes the signal-to-noise ratio and limits the precision of the temperature measurements. The adopted method, instead, employs a temporal

34 4. DATA PROCESSING

average of the images within each run as reference state, and the ratio between this average and instantaneous images is converted to a temperature field via a calibration function. The following sections discuss the two calibration methods available for this experimental setup and illustrate how the temperature fields are extracted.

4.1.2 Absolute temperature calibration

To relate the value of the actual luminescent intensity of the TSP in the RBC cell to absolute temperatures, an in-situ calibration is required. This process involves acquiring images of the TSP at various temperatures while maintaining $T_b \simeq T_t$ and ensuring thermal equilibrium within the fluid sample. A curve of Arrhenius type (Eq. 2.9) is then fitted to these data. Considering that the TSP degrades over the duration of the measurements, an additional correction factor is required. Examination of the plot in Figure 3.6 reveals an initial rapid decay during the first 24 hours (approximately the setup preparation time), after which the degradation rate decreases, suggesting an asymptotic approach to a stable decay value. As no existing studies describe TSP luminescence behaviour after 49 hours of submersion, a linear behaviour was approximated, considering an additional time constant m that accounts for a possible luminescent decay between the measurements. Then, a curve of a modified Arrhenius type (Eq. 2.9) was fitted to the calibration points:

$$I(T_t) = (mt + I_R) \cdot \exp\left[\frac{E_{nr}}{R} \left(\frac{1}{T_t} - \frac{1}{T_R}\right)\right],\tag{4.1}$$

with:

- m: Intensity decay $[sec^{-1}]$;
- t: time [sec];
- T_R : Reference temperature [K];
- I_R : Intensity at temperature T_R ;
- R: Ideal gas constant $[JK^{-1}mol^{-1}]$;
- E_{nr} : Activation Energy $[Jmol^{-1}]$;
- T_t : Top plate temperature [K],

The values I_R , m and E_{nr} are then extracted as fit parameters by fitting Eq. 4.1 to the measured intensities during calibration measurements. The result is a calibration curve which allows conversion of luminescent intensity information into absolute temperatures, accounting for TSP degradation. However, this method suffers from the fact that the TSP intensity decay was found to be non-linear and

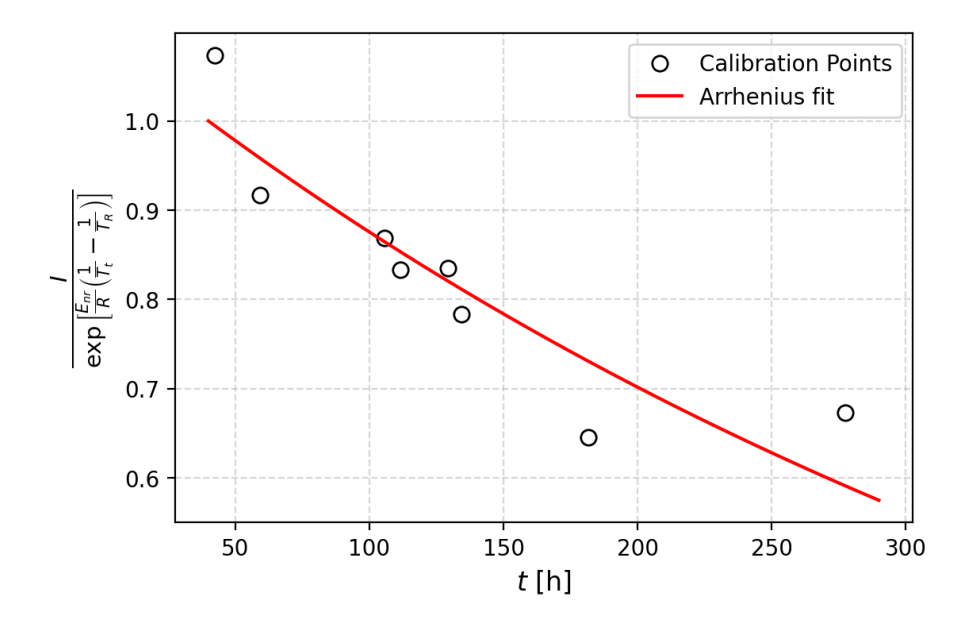


Figure 4.1: Arrhenius fit result of the in-situ calibration for the $\Gamma=4$ volume, illustrating the temporal decay of TSP emission intensity after the start of the measurements (≈ 40 h after submersion). The calibration points exhibit non-monotonic decreasing behaviour upon paint submersion in water for extended periods, and high scatter, resulting in uncertainty in the derived calibration function.

non-monotonic even after 50 hours of submersion with the thinner TSP layer, as shown in Fig. 4.1, where the intensity shows steep decay over 250 hours and the uncertainty of the calibration points does not allow for an accurate fit.

4.1.3 Relative temperature calibration

This method allows for the determination of relative temperature fluctuations with respect to a reference state. It offers the advantage of allowing for an ex-situ calibration in a facility with known and highly controlled boundary conditions. To relate this ex-situ calibration to the TSP in water, reference can be made to the analysis presented in the study by Lemarechal et al. [37], which demonstrated that the TSP sensitivity $\left(\frac{dI(T)}{dT}\right)$ is not altered by exposure to water.

For calibration purposes, during coating of the top plates, reference samples of few centimetres were coated onto aluminium substrates. A new TSP-covered top plate was manufactured for every new sidewalls, i.e., whenever the aspect ratio was changed. Therefore, measurements with different Γ were done with different TSP coatings. Each sample was placed on a heating plate within the PSP/TSP calibration facility at DLR Göttingen. The plate was heated to a determined temperature, and after a calculated time based on the thermal conductivity of the aluminium sub-

36 4. DATA PROCESSING

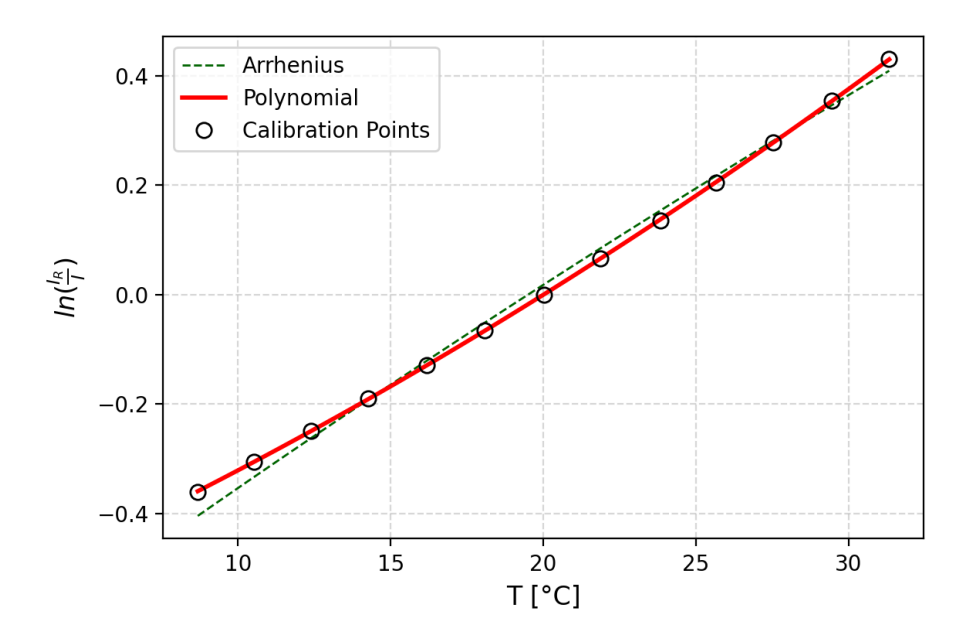


Figure 4.2: Ex-situ calibration data of the sample coated with the TSP used for $\Gamma = 8$; test of different fit functions.

strate, an image of the sample was acquired. For each image, the average intensity was extracted. The calibration points ranged from $10 \, ^{\circ}C$ to $30 \, ^{\circ}C$ with intervals of $2 \, ^{\circ}C$ at ambient pressure. An example of the calibration is displayed in Figure 4.2. To extract a relation between temperature and intensity, the Arrhenius fit was tested but, as shown in the Figure, it did not adequately captured the non-linearity of the data.

A second-order polynomial fit, neglecting the constant term, was then applied:

$$\ln\left(\frac{I_R}{I}\right) = b(T - T_R)^2 + a(T - T_R),\tag{4.2}$$

with:

- T_R : Reference temperature;
- a, b: Polynomial fit coefficients, where a represents the temperature sensitivity at T_R and b its non linear term;
- I: Spatial mean of the TSP signal at temperature T;
- T: Temperature;
- I_R : spatial mean of the TSP signal at T_R .

The fit coefficients a and b were extracted. The fit parameters for the different coatings are listed in Table 4.1. As only the ratio of the intensities enters the calibration function, this method, while in principle allows for calculation of absolute temperatures, it is often used to measure fluctuation relative to a reference state.

Coating #	Γ	a	b
A	4	$(3.87 \pm 0.004) \times 10^{-4}$	$(3.2 \pm 0.07) \times 10^{-4}$
В	8	$(3.78 \pm 0.004) \times 10^{-4}$	$(3.5 \pm 0.06) \times 10^{-4}$
C	16	$(3.36 \pm 0.005) \times 10^{-4}$	$(2.6 \pm 0.07) \times 10^{-4}$
D	32	$(3.48 \pm 0.004) \times 10^{-4}$	$(2.8 \pm 0.06) \times 10^{-4}$

Table 4.1: Polynomial fit coefficients determined for the TSP coatings across different Γ measurements

4.1.4 Spatial calibration

To convert imaging dimensions to physically meaningful lengths, a spatial calibration procedure is performed. This involves determining a scale factor k defined as the ratio of the number of pixels representing each side of the quadratic container to its actual physical dimensions in millimetres. The relative angle of rotation θ of the cell with respect to the camera frame is also accounted for, although this is typically less than 0.3°, as the camera was aligned such that the pixel row and columns are parallel to the sides of the square cell. To obtain coordinates in millimetres, the following transformation is applied:

$$\begin{pmatrix} x \\ y \end{pmatrix} = \frac{1}{k} \begin{pmatrix} x_{px} \\ y_{px} \end{pmatrix} \begin{pmatrix} \cos(\theta) & -\sin(\theta) \\ \sin(\theta) & \cos(\theta) \end{pmatrix}.$$
 (4.3)

Taking as origin the lower left corner of the cell, each axis coordinate is normalised by the height H of the cell.

4.2 Image Processing

4.2.1 Pre-processing

After having selected the relative temperature calibration as suitable method for relating TSP intensities to temperature, the raw images belonging to each run were pre-processed to keep into account the effects described in Chapter 3.3.8, and converted to relative temperature fluctuation fields.

Firstly, the raw intensity images acquired were divided in regions as shown in Fig. 4.3. The main region is the one with the TSP coating (red in Fig. 4.3). The second region is the one corresponding to the cell borders (blue in Fig. 4.3). These regions are distinct, as in some measurements, such as those with $\Gamma = 32$ and $\Gamma = 16$, the TSP layer is not applied to the entire glass plate. Other two regions identified corresponds to the reference paper strips placed at the border outside the

38 4. DATA PROCESSING

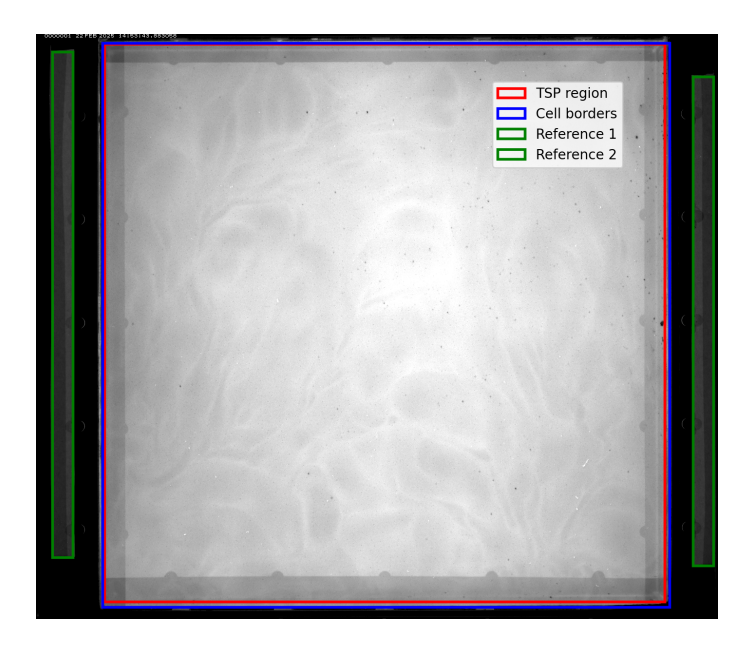


Figure 4.3: A raw image from one of the cases with $\Gamma = 4$. The coloured rectangles mark the cell border (blue), the TSP covered area of the top plate (red) and the two paper strips (green) used as a temperature independent reference to correct for changes in the LED light intensity.

cell, if present ($\Gamma = 8$ and $\Gamma = 4$). To remove the influence of data transfer noise, the "camera dark current" image $\langle I^d \rangle_t$ was subtracted from each image. To account for the intensity decay of the TSP, the temporal evolution of the spatially averaged signal from the TSP region and the one from the reference areas were recorded. The TSP intensity was then normalised by the reference signal (see Section 3.3.8). Assuming a linear decay in TSP intensity over the measurement run, a first-order polynomial was fitted to the resulting data. The slope s of the function represents then the intensity decay. Successively, to each frame of the time-series it was applied

$$I_{ij}^{P} = I_{ij} \cdot \frac{\langle P \rangle_{i,j,t}}{\langle P \rangle_{i,j}} \cdot (1 - s \cdot n), \tag{4.4}$$

where:

- I_{ij}^P : Signal of i, j-th pixel of the pre-processed image;
- I_{ij} : Signal of i, j-th pixel of the raw image;
- $\langle P \rangle_{i,j,t}$: Spatially and temporally averaged reference signal;
- $\langle P \rangle_{i,j}$: Spatially averaged reference signal;
- s: Intensity drift;
- n: Current frame number.

 $\langle P \rangle_{i,j,t}$ was calculated as the average of the last recorded value of the reference

signals from each measurement. After this step, each image within a run is independent from the state of degradation of the TSP or the illumination. In order to generate a reference image to use in the image division procedure and obtain the relative temperature fluctuation fields, the temporal mean of all the corrected images $\langle I_{i,j}^P \rangle_t$ is calculated. This average is performed over a sufficient number of free-fall times to completely remove any coherent structure. $\langle I_{i,j}^P \rangle_t$ therefore accounts for the inhomogeneities of the illumination on the TSP region (such as shadows and bright spots), variations in brightness depending on the local TSP layer thickness, and impurities within the TSP or in the cooling canal (such as static bubbles or rust particles). The average intensity of this image corresponds then to the mean temperature of the TSP with respect to which temperature fluctuations T' can be evaluated.

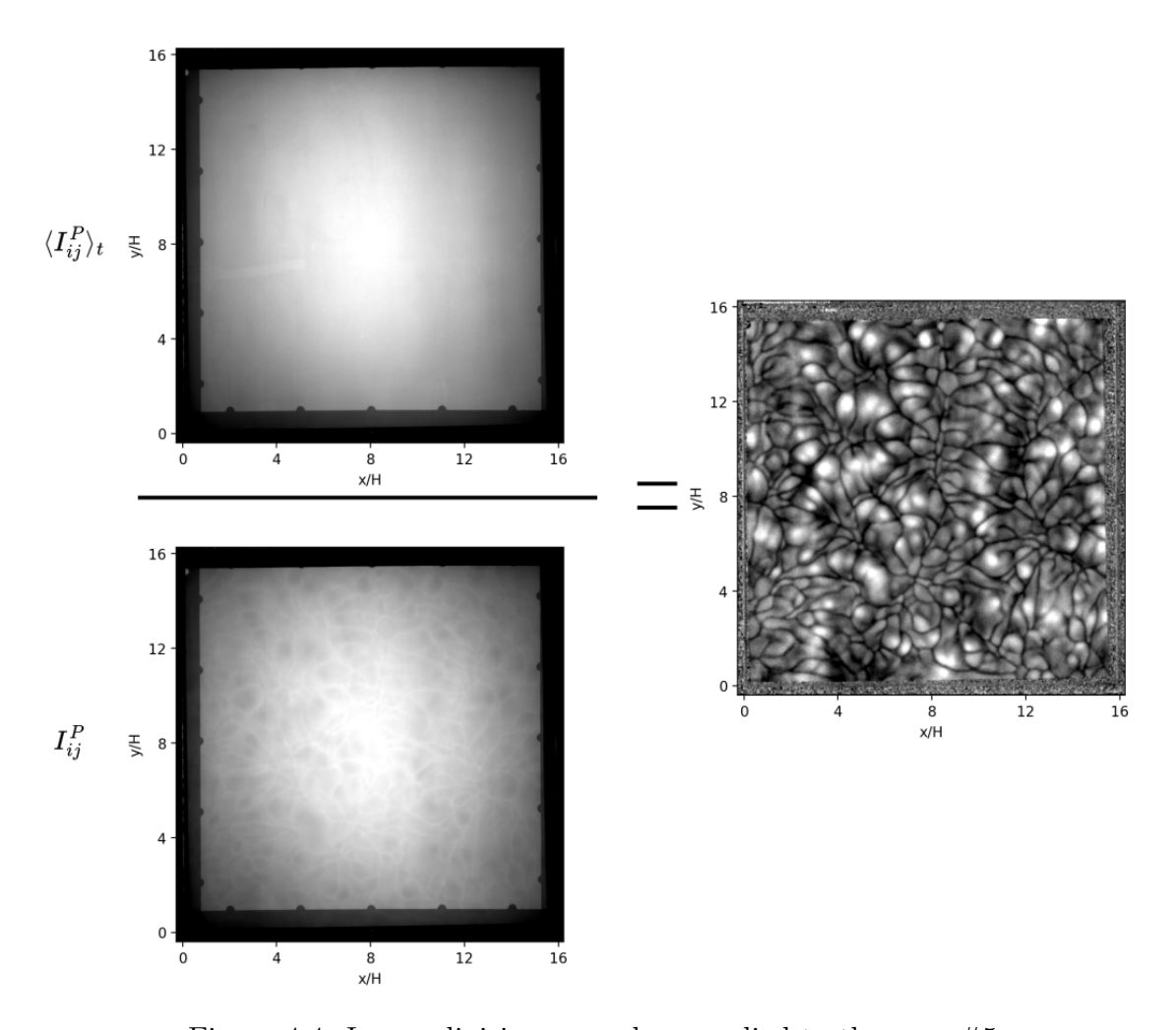


Figure 4.4: Image division procedure applied to the case #5.

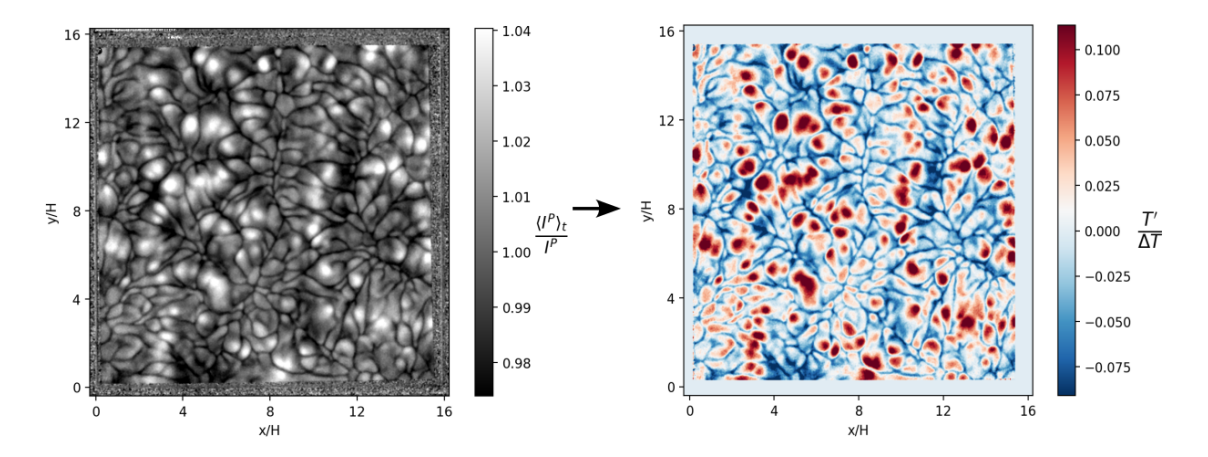


Figure 4.5: Temperature conversion applied to the case #5.

4.2.2 Intensity to temperature conversion

The intensity information was converted to temperatures using Equation 4.2. Here, due to the absence of a reliable calibration curve for the TSP when submerged in water, the value of I_R is not directly available. Therefore, the equation is used to compare I_R to the intensity of each image and to their temporal average:

$$\ln\left(\frac{I_R}{I_{ij}^P}\right) = b(T_{ij} - T_R)^2 + a(T_{ij} - T_R); \tag{4.5}$$

$$\ln\left(\frac{I_R}{\langle I_{ij}^P\rangle_t}\right) = b(T_t - T_R)^2 + a(T_t - T_R),\tag{4.6}$$

where:

- T_{ij} : Temperature at i, j-th pixel;
- T_t : Top plate temperature;
- $\langle I_{i,j}^P \rangle_t$: Temporally averaged signal of i, j-th pixel of pre-processed image.

The two equations were then combined to eliminate I_R and obtain a ratio between the temporally averaged image and each single frame:

$$\ln\left(\frac{I_R}{I_{ij}^P}\right) - \ln\left(\frac{I_R}{\langle I_{ij}^P \rangle_t}\right) = \ln\left(\frac{\langle I_{ij}^P \rangle_t}{I_{ij}^P}\right) = b[(T_{ij} - T_R)^2 - (T_t - T_R)^2] + a(T_{ij} - T_t). \quad (4.7)$$

Herewith, it is assumed that the temperature of the TSP layer amounts to T_t for calculation of the right hand side of the equation, i.e. for evaluation of the sensitivity during calibration. The resulting temperature are still relative to the mean temperature distribution. The ratio $\frac{\langle I_{ij}^P \rangle_t}{I_{ij}^P}$ therefore represents an alternative to the ratio of "wind-off" to "wind-on" images. An example of the image obtained

by performing this operation is displayed in Figure 4.4.

Solving for $T_{i,j} - T_R$ yields,

$$T'_{ij} = T_{ij} - T_R = \sqrt{\left[(T_t - T_R) + \frac{a}{2b} \right]^2 + \frac{1}{b} \ln\left(\frac{\langle I_{ij}^P \rangle_t}{I_{ij}^P}\right)} - \frac{a}{2b}.$$
 (4.8)

The equation has been solved and the images with intensity information I_{ij}^P were converted in images with relative temperature information T'_{ij} . An example of the resulting temperature fluctuation field is shown in Figure 4.5.

Chapter 5

Results

5.1 Main flow features

5.1.1 Instantaneous temperature fields

After processing of the images and their conversion from intensity data to temperature fluctuations, a quantitative analysis of the results can be undertaken to characterise the transition between turbulent regimes dominated by large-scale circulations (LSC) and turbulent superstructures (TSS). Given the large number of data points recorded (Fig. 3.4) and the variety of test-conditions (e.g. different Pr, long-term evolution, transient scenarios), the cases considered in the current study are restricted to a subset for the sake of brevity. The covered parameter space is summarised in Figure 5.1, and the corresponding conditions are listed in Tab. A.1. Herewith, most of them were conducted at Pr = 7, but some measurements were performed at elevated T_m to prevent condensation on the cooling plate.

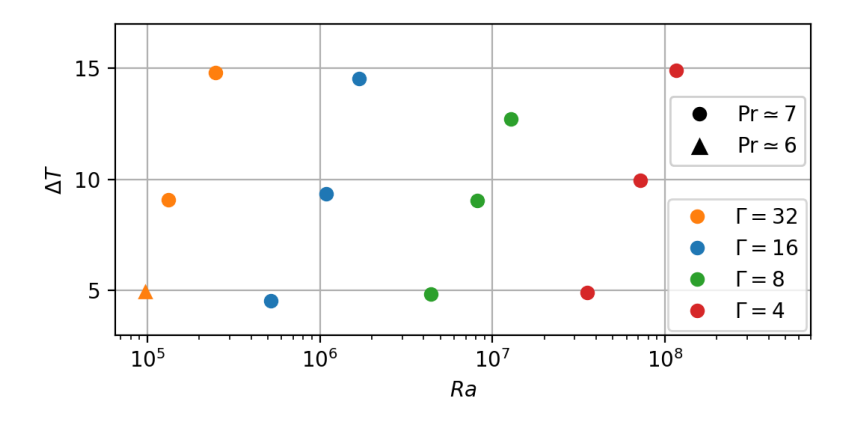


Figure 5.1: Parameter space considered for the analysis. Detailed values are given in Tab. A.1.

5. RESULTS

Figure 5.2 provides an overview of instantaneous temperature fields for each experimental run. The colour scale in the figure represents positive temperature fluctuations relative to the reference state as shades of red, and negative fluctuations as shades of blue. Positive fluctuations typically exhibit a rounded shape and are attributable to warm, upwelling fluid. They are surrounded by blue regions that stand out due to their thin structures. They can be interpreted as fingerprints of the cold thermal plumes, that are ejected from the thermal boundary layer. Analysing the time series, it is observed that the warm structures diverge towards the cold ones, indicating that the fluid is cooling down while flowing along the top plate.

While the thermal structures appear similar to a certain extent in the various flow cases, they exhibit different characteristics when looking in more detail regarding their number, size and alignment, which are elaborated on the following paragraph. The discussion starts from the first row in Fig. 5.2, which displays results for $\Gamma = 32$ and the lowest Ra. For all the Ra, the regions of upwelling warm fluid organise themselves into linear arrangements, that form polygonal structures. The latter define the domain walls of larger convection cells and encompass regions with sinking cold fluid. Herewith, the high visibility of these cells already in the instantaneous fields allows to estimate their wavelength, which amounts to approximately 7H. Few regions of upwelling fluid are concentrated along the sidewalls, and most convection cells appear to be sharply truncated by them, suggesting that the interaction between the two is weak or negligible. The polygonal structures take different shapes, ranging from triangles to pentagons, and, as with patterns at the onset of convection, tend to align with the container walls, as is particularly evident in Fig. 5.2(c). Increasing Ra does not notably alter the wavelength of the structures, but rather blurs the warm alignments due to an increase in the number of smaller warm regions along their sides, resulting in a consequent decrease in the size of the colder regions. Fig. 5.2 (d,e,f), with $\Gamma = 16$, displays structures with similar features as $\Gamma = 32$, however less ordered. In particular, the warm round regions are less coherently aligned. The convection cells at lower Ra are still visible enough to estimate their wavelength being slightly larger than 5H. Further increase in Ra causes smaller warm regions to appear aside the larger, aligned ones, and renders the structures less defined. Consequently, the size of the few visible convection cells seems to decrease. At $\Gamma = 8$, the regions of warm upwelling fluid do not reveal any obvious geometric arrangements any more. Furthermore, they are more evenly distributed over the cooling plate. However, some faint arrangements can be recognised, although they do not develop into complete convection cells in the instantaneous temperature fluctuation fields. At $\Gamma = 4$ finally, only few and sparse warm regions can be recognised, and no alignments in the temperature fluctuations are discernible anymore (see Fig.5.2 (j,k,l)). The fact that most of the fluid with high positive fluctuation is concentrated near the lateral boundaries or in the corners is considered as an indication of strong side-wall interaction.

In the following, the temporal evolution of the temperature fluctuation fields as observed in the time series will be discussed. Beginning again with $\Gamma = 32$, see Fig. 5.2 (a,b,c), significant temperature variations are mostly observable in the

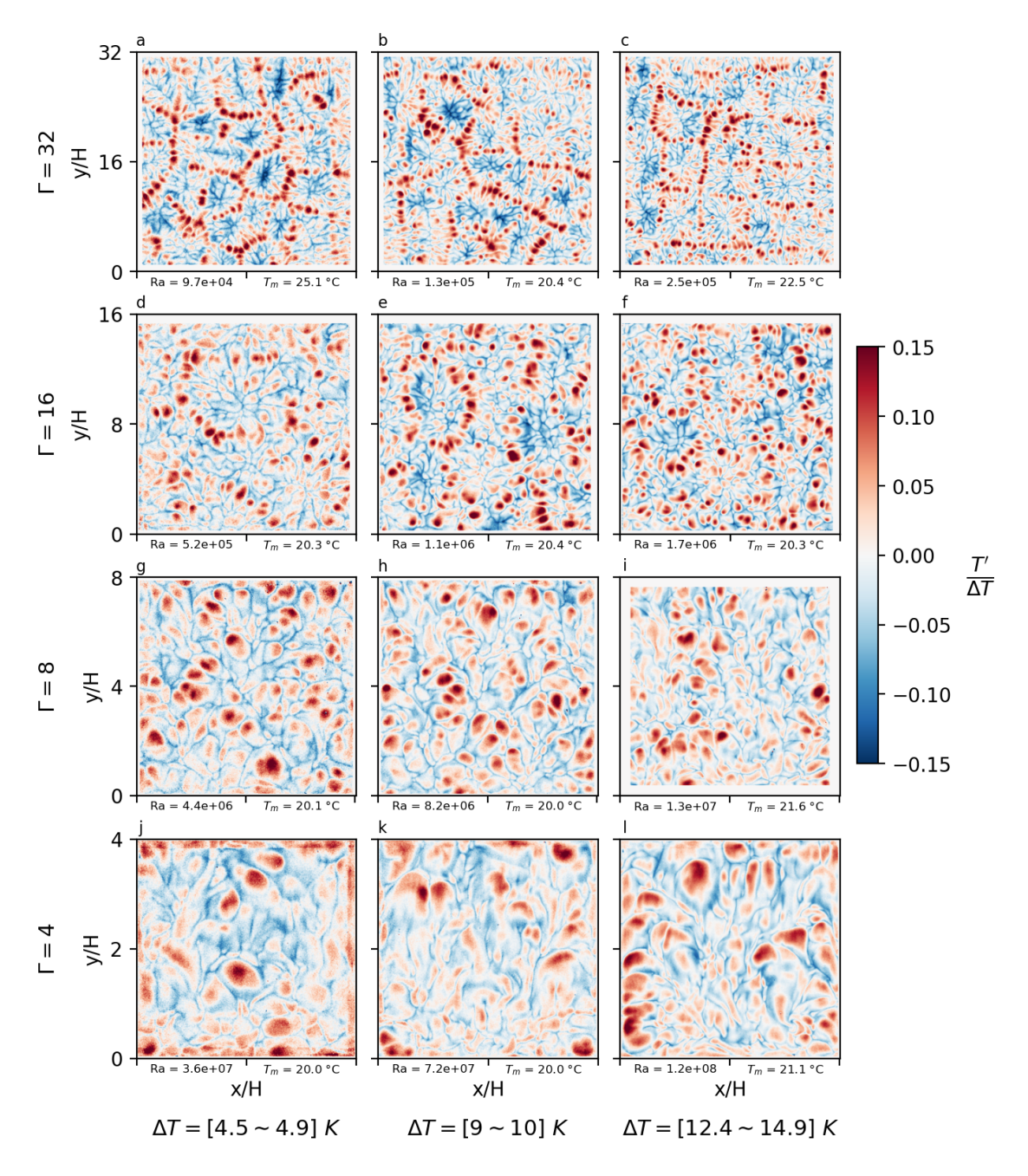


Figure 5.2: Overview of instantaneous temperatures field over the different test cases, sorted with respect to Γ and ΔT .

46 5. RESULTS

small-scale patterns whereas the large-scale structures are rather stable in time: the convection cells smoothly reorient and adopt different shapes without sudden events. With increasing Ra, the frequency of the lateral oscillation of the smaller red regions appearing alongside the warm alignments rises. At $\Gamma = 16$, the convection cells, still visible in the snapshots, become highly transient and reorientate continuously within ~ 50 free-fall times t_f . At $\Gamma = 8$, the temporal evolution of the flow becomes highly dynamic in the sense that the regions of warm upwelling fluid are appearing and disappearing within few t_f , and are displaced randomly throughout the domain. At $\Gamma = 4$, finally, the flow is fully chaotic. Large warm plumes impact the top plate and spread across it, but their origin is not fixed in space and varies frequently in time. However, hidden in these small and intermediate fluctuations, large scales structures spanning a part or even the complete sample can be identified, as e.g. a dual roll structure in Fig. 5.2(1), that originates from upwelling fluid at the sidewalls at the lateral sides of the figure and downwelling fluid in the centre. Throughout the run, the flow undergoes many events, such as shifting and rotation of the rolls.

5.1.2 Averaged temperature fields

Averaging multiple snapshots over a specific time duration, as described in Chapter 2.1, allows to separate the rapid fluctuations from the slowly-evolving TSS, high-lighting their respective contributions. In Weiss et al. [23], a time-scale suitable for isolating the TSS has been determined to be 50 free-fall times at $Ra = 1.1 \times 10^6$. Accordingly, Fig. 5.3 shows the averages of the temperature fluctuation fields over 50 t_f for the different flow cases. Before going into the detailed discussion of each Γ , it should be noted that the magnitude of the positive and negative fluctuation decreases with increasing Ra (and decreasing Γ), pinpointing to a diminishing temporal stability or lifetime of the coherent structures.

At $\Gamma=32$, individual circular warm regions are expectedly still discernible due to the high temporal stability of the convection cells. This result appears largely independent of Ra as the structures remain well-defined across the three different cases shown. However, as for the other aspect ratios, averaging allows for a clearer identification of the structures' wavelength, shape, and alignment. In the centre of the convection cells, regions of negative fluctuations form lines converging towards central points, indicating a rather stable alignment and localisation of the cold plumes over 50 free-fall times as well. At $\Gamma=16$, by averaging the instantaneous temperature fluctuation fields, structures that were hardly discernible in the instantaneous fields become visible, such as the polygonal structure at the lower-right corner of Fig. 5.3(d). At the lower Ra the structures exhibit sufficient clarity

for a more precise assessment of their size. Upon incrementing Ra, the walls of the polygonal convection cells become less distinct, and eventually, at higher Ra some break down and evolve into larger, more turbulent convection cells, as observed at the bottom of Fig. 5.3(f). At $\Gamma = 8$, averaging allows highlighting, albeit faintly, of some long-lived structures previously not observable in the instantaneous tempera-

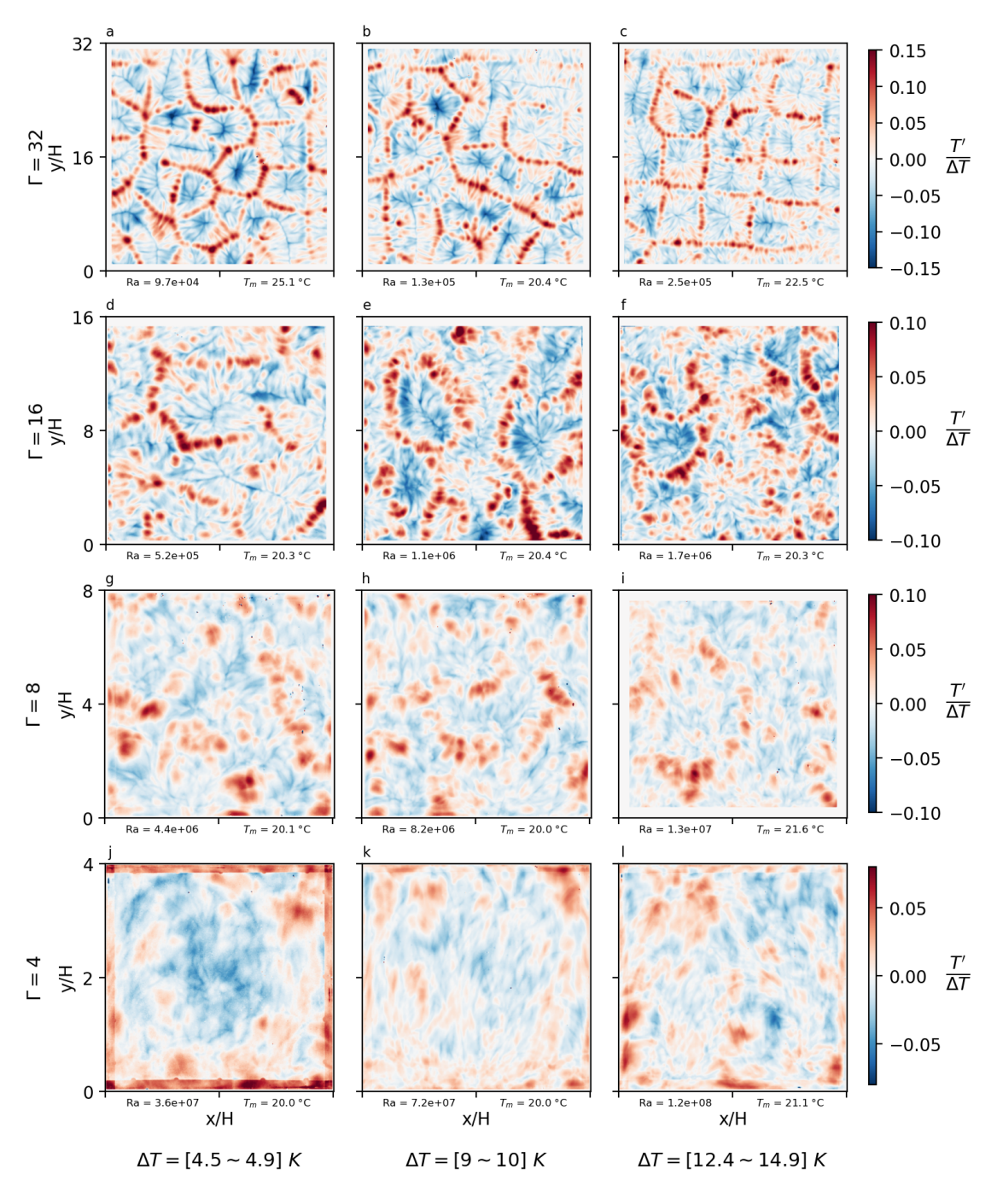


Figure 5.3: Overview of the mean temperature fields, averaged over 50 t_f . The test conditions are sorted with respect to Γ and ΔT .

48 5. RESULTS

ture fields or the time series. In fact, it is possible to recognise convection cells in Fig. 5.3(h) and 5.3(i). Interestingly, some areas of the flow in Fig. 5.3(g) resemble the features observed in Fig. 5.3(f), i.e. the highest Ra for $\Gamma=16$. The results for $\Gamma=4$, finally, reveal a largely homogeneous averaged temperature field, attributable to the high turbulence and increased mixing of flow features. However, extended regions of warm fluid (mostly close to the lateral boundaries) and cold fluid (mostly in the central part) indicate the occurrence of large scale circulations. For example, the flow in Fig. 5.3(j) reveals a toroidal motion, whereas in Fig. 5.3(k), two rolls can be spotted from upwelling fluid on the upper and lower side and a sink in the central region. The flow in Fig. 5.3(l), however, is more complex, involving multiple large circulations. Being averaged over 50 free-fall times, these flow structures still represent transient structures, which evolve over time and change between a variety of characteristic combination of LSC.

5.2 Statistical analysis

In order to obtain a quantitative and statistically comprehensive view on the experimental results, probability density functions (PDFs) of the temperature fluctuation fields were calculated considering the complete data set for each run. Selected results are presented in Fig. 5.4, for varying Γ at a fixed $\Delta T = 10$ K, alongside with a Gaussian distribution with standard deviation $\sigma = 0.06$, related to the one of the temperature field of measurement #2 with $\Gamma = 32$ and $\Delta T = 10$ K.

The PDFs of the instantaneous fields (Fig. 5.4(a)) exhibit a similar width across all aspect ratios, with standard deviation of approximately $\sigma=0.05$. The PDF for $\Gamma=32$ is the broadest, while, with decreasing Γ (and therefore increasing Ra), the curves narrow. The negative tails exhibit a decline whose steepness depends on Γ , although not with a strictly monotonic dependence. On the positive half, instead, they follow a broadly similar behaviour. A general positive skewness of approximately 1.6 is observed, which is expected as the measurement is performed at the cooling plate, hence with a rigid wall on one side and convecting fluid on the other.

Averaging the fluctuation fields over 50 t_f , as done in Fig. 5.3, allows to filter out the rapid temperature fluctuations. The PDFs of these filtered fields (5.4(b)) are significantly narrowed as compared to those of the raw fluctuations. This trend indicates a diminishing temporal stability or lifetime of coherent structures with decreasing Γ and increasing Ra. Interestingly, upon this averaging process, the distributions remain skewed of approximately 1.8. Herewith, the PDF for $\Gamma = 32$ is

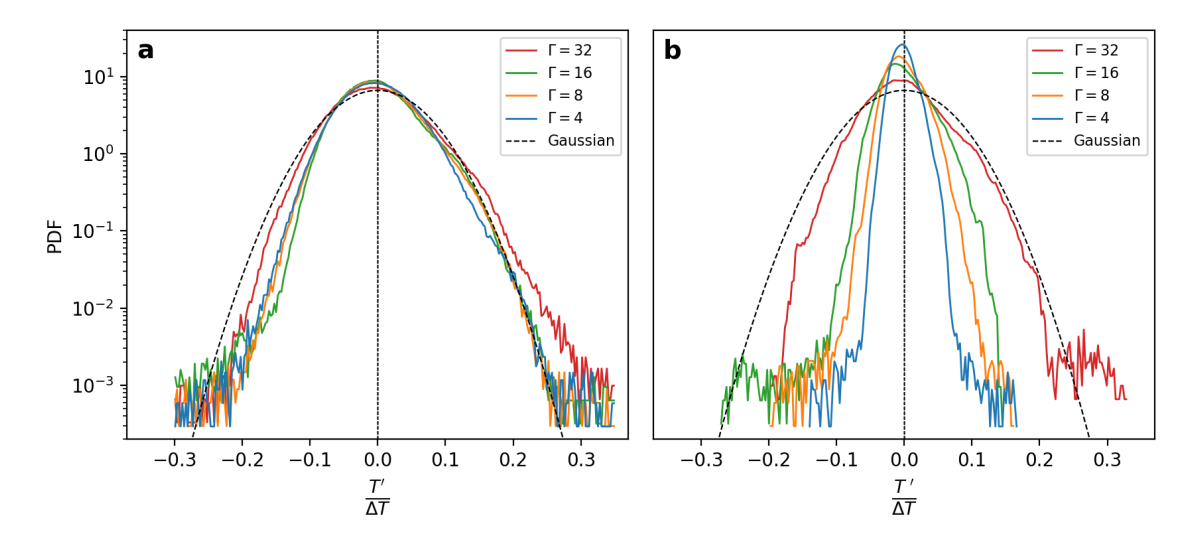


Figure 5.4: Probability density functions of instantaneous temperature fluctuations (a) and fluctuation from averages over 50 t_f (b) for different aspect ratios at $\Delta T = 10K$.

altered the least, exhibiting only a slight decrease of higher fluctuation magnitudes. The negative tail of the curve is cut at a lower magnitude, as compared to the positive tail, suggesting higher temporal stability of the warm structures as compared to the cold ones. With decreasing Γ , the impact of the filtering on the PDFs becomes more pronounced, while the skewness of the PDFs is retained, as already stated. At $\Gamma = 4$ finally, the averaged PDF results narrowed down to $\sigma = 0.02$, indicative of a temperature field dominated by rapid, short-lived fluctuations.

5.3 Comparison with other measurements and DNS

As this represents the first study that applies TSP to study RBC, it is worthwhile to compare the results to data available in the literature from comparable studies.

Recently, Weiss et al. [23] employed the same RBC setup as used in the current study to measure the volumetric velocity field in the fluid using Lagrangian particle tracking (LPT). Figure 5.5 depicts an instantaneous temperature fluctuation field from case #5 of the current study (see Table 4.1) side-by-side with a plot of the vertical velocities by Weiss et al. [23] in a horizontal slice above the bottom plate at z = 0.1/H. As expected, given the opposing measurement planes, the flow features are complementary: the LPT data reveals cold downwelling fluid, while the TSP measurements show warm upwelling fluid defining the convection cells. Despite depicting different quantities from different positions in the fluid, the observed coherent structures are strikingly similar, given the strong coupling between tem-

50 5. RESULTS

perature and vertical velocity in the boundary layers. Naturally, the structures have opposite sign. Besides that, TSS as well as thermal plumes can be clearly recognised, and the coherent structures result of comparable dimensions in the TSP and LPT data sets. While LPT provides highly resolved measurements of velocities and accelerations in the volume, and TSP measures thermal imprints at the surface with high spatial and temporal resolution, the different measurements techniques reveal complementary views on the large and small scale structures in the RBC experiment in study. Combining the findings from these techniques can hence allow for a more comprehensive understanding of RBC and the observed turbulent structures.

Another comparison can be drawn between the TSP measurements in the current study and the direct numerical simulation (DNS) by Pandey et al. [20] in a volume with $\Gamma = 25$, at Pr = 7 and $Ra = 10^5$, see Fig. 5.6. It should be noted, though, that the TSP results are given as temperature fluctuation fields, as before, while the DNS visualises the temperature derivative at the wall. The latter was performed applying isothermal boundary conditions at the bottom and top plates, with thermally insulated sidewalls and no-slip condition. Consequently, a direct comparison of wall temperatures is not meaningful, as the DNS, by definition, does not exhibit thermal structures on the heating plates. Nevertheless, this comparison is pertinent, as both TSP and the DNS data analysed here are highly related to the local heat flux. As a result, at first glance, striking similarities in the structures

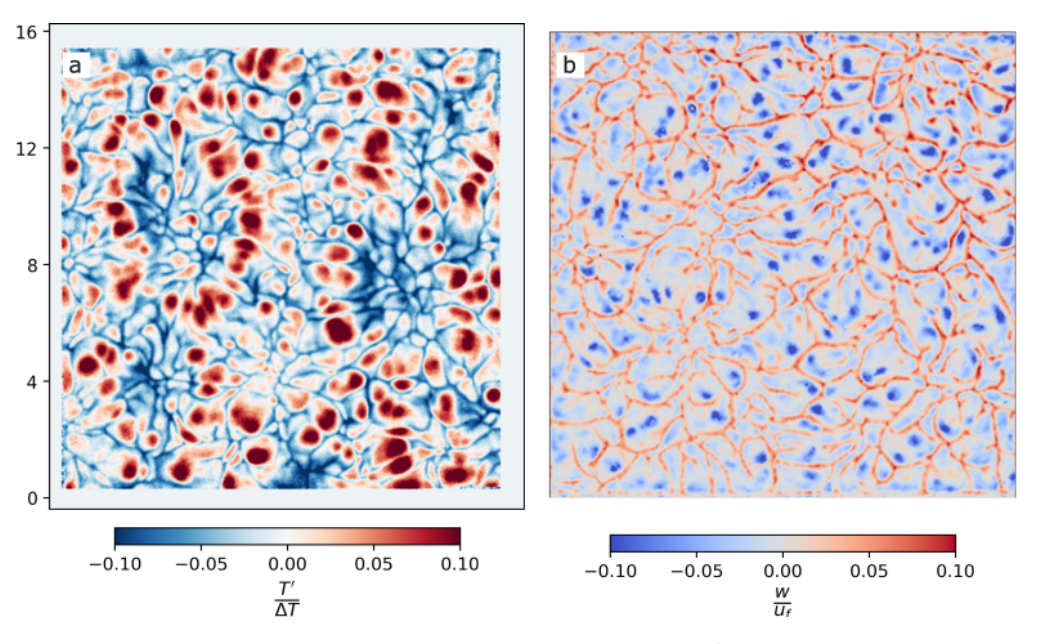


Figure 5.5: Two snapshots of RBC with $Ra = 1.1 \times 10^6$ and Pr = 7. Snapshot (a) represents the temperature fluctuations on the cooling plate measured with TSP, while snapshot (b) represents the vertical velocity component measured using LPT by Weiss et al. [23] close to the bottom plate at z = 0.1/H.

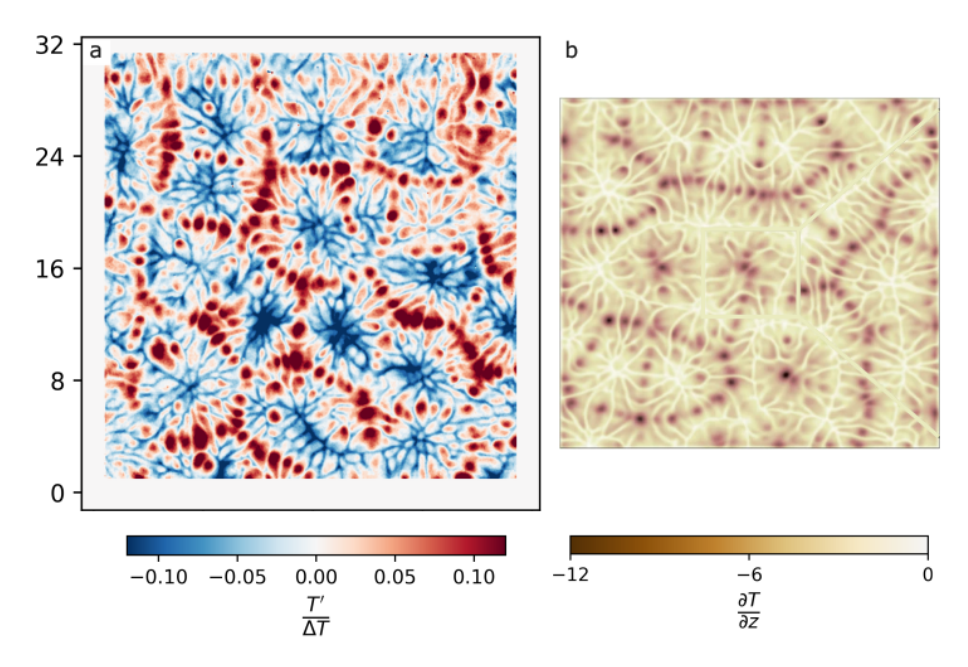


Figure 5.6: Comparison of instantaneous temperature data. (a) Temperature fluctuations on the cooling plate measured with TSP at $\Gamma=32$, (b) vertical temperature gradient on the heating plate from DNS by Pandey et al. [20] with $\Gamma=25$, $Ra=10^5$ and Pr=7. The fields are depicted at the same spatial scale for comparison.

can be observed. The warm upwelling fluid regions display similar circular shapes and sizes, and in both datasets, these regions align to form polygonal structures. The thermal line plumes ejected from the thermal boundary layer are also visible in both temperature fields. In both results, few warm regions are concentrated along the sidewalls, with the convection cells showing little interaction with them. Specifically, it is observed in results (a) and (b) that the domain walls of the convection cells, at least one face of each polygon, are aligned with the container walls. In case (a), the cells are predominantly pentagonal or squared in shape, a trend also observed in case (b). Finally, the polygonal structures are very similar in size too. However, a more detailed investigation is required to quantify this observation with high statistical relevance.

5.4 Final discussion and summary

In the current chapter, temperature fluctuation fields of a selected subset of test-cases comprising three similar temperature differences (5, 10 and 15 K) at aspect ratios 32, 16, 8 and 4 were presented and discussed qualitatively and, in certain aspects, quantitatively. Besides the PDF of the temperature fluctuations, the shape, size, and alignment of coherent structures were analysed in both instantaneous and

52 5. RESULTS

averaged temperature fields. Considering the temporal evolution in the time-series, the dynamic evolution and temporal stability of the coherent structures were elaborated upon. Integrating these observations already allows for a preliminary classification of the flow regimes with respect to the question whether they are dominated by pattern, turbulent superstructures (TSS) or large-scale circulations (LSC).

At $\Gamma = 32$, especially at the two lower Ra, the temperature fluctuation fields exhibited well-defined polygonal structures formed by upwelling warm fluid, with wavelengths smaller than the lateral sample size L. These structures displayed minimal interaction with the sidewalls and shined out with high temporal stability, undergoing only smooth and limited rearrangements. Averaging over 50 t_f further enhanced the visibility of these structures by filtering out rapid fluctuations. The temporal stability was further confirmed by the PDF analysis, which revealed only a minimal alteration by the averaging process. These characteristics are often indicative of a predominantly time-dependent pattern flow. At the highest measured Ra for this Γ , these polygonal structures became slightly less discernible in the instantaneous fields; however, the averaging procedure revealed again the underlying pattern. At $\Gamma = 16$, the flow became increasingly turbulent, and the arrangement of warm regions was more difficult to determine in the instantaneous snapshots. Nevertheless, averaging highlighted the polygonal structures, allowing for a more precise assessment of their shape and size and suggesting that these structures evolve into TSS, partially overshadowed and frequently rearranged by the turbulent flow. With increasing Ra, the structures became less pronounced and even localised breakdown could be observed. At $\Gamma = 8$, a higher number of warm fluid regions exhibited interaction with the sidewalls. Coherent structures were barely recognisable in instantaneous snapshots, and averaging revealed only a few longer-lived structures, suggesting transition from TSS to LSC. Finally, at $\Gamma = 4$, no coherent structures were observable in either the instantaneous temperature snapshots or the averaged fields. This absence of discernible structures was a direct consequence of the significant constraint imposed by the sidewalls, which strongly interact with the flow and dictate its circulation pattern. The flow, as expected, is here characterised by a clear dominance of LSC.

In summary, a transition from time-dependent flow to turbulent flow was observed between the measurements with $\Gamma=32$ and $\Gamma=16$, occurring between $Ra=2.5\times 10^5$ and $Ra=5.2\times 10^5$. This transition broadly corresponds to that identified by Krishnamurti [11] in the regime diagram shown in Fig. 2.2. Furthermore, a smooth evolution from TSS to LSC was observed from $\Gamma=16$ to $\Gamma=8$, occurring between $Ra=1.7\times 10^6$ and $Ra=4.4\times 10^6$, and with increasing Ra at

 $\Gamma=8.$ Finally, at $\Gamma=4,$ the flow is completely dominated by LSC.

Chapter 6

Conclusions

This study on the application of temperature sensitive paint to a Rayleigh-Bénard convection volume presented several novel challenges.

Firstly, achieving ideal boundary conditions, typically difficult in any RBC experimental setup, necessitated a thorough assessment of their thermal uniformity. Secondly, the unconventional use of high-power LEDs for long-term measurements, along with their non-linear behaviour throughout the acquisitions, required the implementation of reference signals to account for these effects in post-processing. Lastly, the limited existing literature regarding TSP behaviour when submerged in water necessitated a new characterisation of the paint performance and tracking of its properties throughout the measurement campaigns. Addressing these effects led to the development of a precise calibration method capable of accurately relating the paint luminescent intensity to temperature fluctuations relative to a reference state. This calibration allowed for the conversion of the raw images into temperature fields underneath the top plate in Rayleigh-Bénard convection at varying Γ and different Ra. The results are rich in information, and provides excellent visualisation of the thermal imprint of flow structures at the fluid sample's top plate with high spatial and temporal resolution. Qualitative and quantitative observations of the flow features already reveal multiple interesting dynamics, and initial conclusions regarding the transition between turbulent superstructures and large-scale circulation can be drawn. Moreover, the comparison with existing experimental and numerical data demonstrate the TSP's ability to capture flow structures consistent with previous studies of RBC. Many opportunities for further investigation remain, such as measurements of autocorrelation to extract temporal and spatial power spectral densities, that can bring information on the structures' wavelengths, and analysis of cross-correlation to assess their stability in time. Furthermore, proper orthogonal decomposition (POD) could be employed to isolate the dominant modes of the flow, 56 6. CONCLUSIONS

providing an even deeper understanding of the flow physics.

Appendix A

Appendix

58 A. APPENDIX

	t_{η} [s]	1.30	1.07	0.69	1.69	1.04	0.78	1.66	1.10	0.82	1.70	1.08	0.79
	η [mm] η	1.08	1.03	0.81	1.30	1.02	0.88	1.29	1.05	0.89	1.30	1.04	0.88
	τ_{total}	4000	4900	0099	2100	5100	2600	1770	2300	3000	1200	1800	2200
	$u_f[\frac{\mathrm{cm}}{\mathrm{s}}]$	1.12	1.37	1.84	1.36	1.96	2.45	1.98	2.71	3.52	2.82	4.02	5.05
runs	Duty cycle [%]	10	10	10	10	10	20	20	20	20	40	40	40
Measurement runs	Framerate [Hz]	1	1	1	1	1	2	2	2	2	4	4	4
	$q[rac{\mathrm{W}}{\mathrm{m}^2}]$	066	2190	4100	820	2020	3470	860	1800	2880	092	1830	3020
	Pr	6.1	6.9	6.5	7.0	6.9	6.9	7.0	7.0	6.7	7.0	7.0	6.8
	Ra	9.7×10^{4}	1.3×10^5	2.5×10^5	5.2×10^5	1.1×10^6	1.7×10^6	4.4×10^{6}	8.2×10^6	1.3×10^7	3.6×10^7	7.2×10^7	1.2×10^8
	$\Delta T [\mathrm{K}]$	4.95	60.6	14.79	4.52	9.30	14.55	4.80	9.00	12.40	4.91	96.6	14.89
	Ĺ	32	32	32	16	16	16	∞	∞	∞	4	4	4
	#	Н	2	က	4	ಬ	9	7	∞	6	10		12

Table A.1: Experimental parameters and characteristic quantities of the runs considered interesting. The table displays the aspect ratio Γ , the temperature gradient ΔT , the Rayleigh number Ra, the Prandtl number Pr, the heat flux density q, the framerate of acquisition, the duty cycle of the LEDs pulse, the free-fall velocity u_f , the total number of free-fall times recorded τ_{total} , as well as the Kolmogorov length η and time scale t_{η} .

Bibliography

- [1] H. Bénard. "Les tourbillons cellulaires dans une nappe liquide. Méthodes optiques d'observation et d'enregistrement". In: *J. Phys. Theor. Appl.* 10.1 (1901), pp. 254–266. DOI: 10.1051/jphystap:0190100100025400. URL: https://hal.science/jpa-00240502.
- [2] L. Rayleigh. "LIX. On convection currents in a horizontal layer of fluid, when the higher temperature is on the under side". In: *The London, Edinburgh, and Dublin Philosophical Magazine and Journal of Science* 32.192 (1916), pp. 529–546. DOI: 10.1080/14786441608635602.
- [3] P. Manneville. "Rayleigh-Bénard Convection: Thirty Years of Experimental, Theoretical, and Modeling Work". In: vol. 207. June 2010, pp. 41–65. ISBN: 978-0-387-40098-3. DOI: 10.1007/978-0-387-25111-0_3.
- [4] G. Ahlers, D. S. Cannell, V. Steinberg. "Time Dependence of Flow Patterns near the Convective Threshold in a Cylindrical Container". In: *Phys. Rev. Lett.* 54 (13 Apr. 1985), pp. 1373–1376. DOI: 10.1103/PhysRevLett.54.1373. URL: https://link.aps.org/doi/10.1103/PhysRevLett.54.1373.
- [5] H. Jeffreys. "Some cases of instability in fluid motion". In: Proceedings of the Royal Society of London. Series A, Containing Papers of a Mathematical and Physical Character 118.779 (1928), pp. 195-208. DOI: 10.1098/rspa.1928. 0045. URL: https://royalsocietypublishing.org/doi/abs/10.1098/ rspa.1928.0045.
- [6] W. H. Reid, D. L. Harris. "Some Further Results on the Bénard Problem". In: Physics of Fluids 1.2 (1958), pp. 102–110. DOI: 10.1063/1.1705871. URL: https://doi.org/10.1063/1.1705871.
- [7] Z.-H. Wan, P. Wei, R. Verzicco, D. Lohse, G. Ahlers, R. J. A. M. Stevens. "Effect of sidewall on heat transfer and flow structure in Rayleigh-Bénard convection". In: *Journal of Fluid Mechanics* 881 (2019), pp. 218–243. DOI: 10.1017/jfm.2019.770.

60 BIBLIOGRAPHY

[8] O. Shishkina. "Rayleigh-Bénard convection: The container shape matters". In: *Phys. Rev. Fluids* 6 (9 Sept. 2021), p. 090502. DOI: 10.1103/PhysRevFluids. 6.090502. URL: https://link.aps.org/doi/10.1103/PhysRevFluids.6.090502.

- [9] M. C. Cross, P. C. Hohenberg. "Pattern formation outside of equilibrium". In: Rev. Mod. Phys. 65 (3 July 1993), pp. 851-1112. DOI: 10.1103/RevModPhys. 65.851. URL: https://link.aps.org/doi/10.1103/RevModPhys.65.851.
- [10] P. Sakievich, Y. Peet, R. Adrian. "Large-scale thermal motions of turbulent Rayleigh-Bénard convection in a wide aspect-ratio cylindrical domain". In: International Journal of Heat and Fluid Flow 61 (2016). SITSFP9 special issue, pp. 183–196. ISSN: 0142-727X. DOI: https://doi.org/10.1016/j.ijheatfluidflow.2016.04.011. URL: https://www.sciencedirect.com/science/article/pii/S0142727X16301461.
- [11] R. Krishnamurti. "On the transition to turbulent convection. Part 2. The transition to time-dependent flow". In: *Journal of Fluid Mechanics* 42.2 (1970), pp. 309–320. DOI: 10.1017/S0022112070001283.
- [12] G. Ahlers. "Turbulent Convection". In: *Physics* 2 (2009), p. 74. DOI: 10.1103/ Physics.2.74. URL: https://doi.org/10.1103/Physics.2.74.
- [13] J. Bosbach, D. Schanz, P. Godbersen, A. Schröder. "Dynamics of Coherent Structures in Turbulent Rayleigh-Bénard Convection by Lagrangian Particle Tracking of Long-Lived Helium Filled Soap Bubbles". In: July 2022.
- [14] G. Paolillo, C. S. Greco, T. Astarita, G. Cardone. "Experimental determination of the 3-D characteristic modes of turbulent Rayleigh-Bénard convection in a cylinder". In: *Journal of Fluid Mechanics* 922 (2021), A35. DOI: 10.1017/jfm.2021.554.
- [15] L. P. Kadanoff. "Turbulent Heat Flow: Structures and Scaling". In: Physics Today 54.8 (Aug. 2001), pp. 34–39. ISSN: 0031-9228. DOI: 10.1063/1.1404847. eprint: https://pubs.aip.org/physicstoday/article-pdf/54/8/34/16746047/34_1_online.pdf. URL: https://doi.org/10.1063/1.1404847.
- [16] X.-D. Shang, X.-L. Qiu, P. Tong, K.-Q. Xia. "Measured Local Heat Transport in Turbulent Rayleigh-Bénard Convection". In: *Phys. Rev. Lett.* 90 (7 Feb. 2003), p. 074501. DOI: 10.1103/PhysRevLett.90.074501. URL: https://link.aps.org/doi/10.1103/PhysRevLett.90.074501.

- [17] P. Oresta, G. Stringano, R. Verzicco. "Transitional regimes and rotation effects in Rayleigh-Bénard convection in a slender cylindrical cell". In: *European Journal of Mechanics B/Fluids* 26.1 (2007), pp. 1–14. ISSN: 0997-7546. DOI: https://doi.org/10.1016/j.euromechflu.2006.04.006. URL: https://www.sciencedirect.com/science/article/pii/S0997754606000707.
- [18] J. Cuba, M. S. Emran, J. Schumacher. "Aspect ratio dependence of heat transfer and large-scale flow in turbulent convection". In: *Journal of Fluid Mechanics* 655 (2010), pp. 152–173. DOI: 10.1017/S0022112010000820.
- [19] R. J. A. M. Stevens, A. Blass, X. Zhu, R. Verzicco, D. Lohse. "Turbulent thermal superstructures in Rayleigh-Bénard convection". In: *Phys. Rev. Fluids* 3 (4 Apr. 2018), p. 041501. DOI: 10.1103/PhysRevFluids.3.041501. URL: https://link.aps.org/doi/10.1103/PhysRevFluids.3.041501.
- [20] A. Pandey, J. D. Scheel, J. Schumacher. "Turbulent superstructures in Rayleigh-Bénard convection". In: *Nature Communications* 9.1 (2018). DOI: 10.1038/s41467-018-04478-0. URL: https://www.nature.com/articles/s41467-018-04478-0.
- [21] S. Moller, C. Resagk, C. Cierpka. "Long-time experimental investigation of turbulent superstructures in Rayleigh-Bénard convection by noninvasive simultaneous measurements of temperature and velocity fields". In: *Experiments in Fluids* 62.64 (2021). DOI: 10.1007/s00348-020-03107-1. URL: https://link.springer.com/article/10.1007/s00348-020-03107-1.
- [22] S. Moller, T. Käufer, A. Pandey, J. Schumacher, C. Cierpka. "Combined particle image velocimetry and thermometry of turbulent superstructures in thermal convection". In: *Journal of Fluid Mechanics* 945 (2022), A22. DOI: 10.1017/jfm.2022.538.
- [23] S. Weiss, D. Schanz, A. O. Erdogdu, A. Schröder, J. Bosbach. "Investigation of turbulent superstructures in Rayleigh-Bénard convection by Lagrangian particle tracking of fluorescent microspheres". In: Experiments in Fluids 64 (2023). DOI: 10.1007/s00348-023-03624-9. URL: https://link.springer.com/ article/10.1007/s00348-023-03624-9.
- [24] M. Ghazijahani, C. Cierpka. "Spatio-temporal dynamics of superstructures and vortices in turbulent Rayleigh-Bénard convection". In: *Physics of Fluids* 36.3 (Mar. 2024), p. 035120. ISSN: 1070-6631. DOI: 10.1063/5.0191403. eprint: https://pubs.aip.org/aip/pof/article-pdf/doi/10.1063/5.0191403/19716786/035120_1_5.0191403.pdf. URL: https://doi.org/10.1063/5.0191403.

62 BIBLIOGRAPHY

[25] T. Liu, J. P. Sullivan, K. Asai, C. Klein, Y. Egami. *Pressure and Temperature Sensitive Paints. Second Edition*. Ed. by W. Merzkirch, D. Rockwell, C. Tropea. Experimental Fluid Mechanics. Cham: Springer International Publishing, 2021, pp. xviii + 542. ISBN: 978-3-030-68056-5. DOI: 10.1007/978-3-030-68056-5.

- [26] V. Ondrus, R. J. Meier, C. Klein, U. Henne, M. Schäferling, U. Beifuss. "Europium 1,3-di(thienyl) propane-1,3-diones with outstanding properties for temperature sensing". In: Sensors and Actuators A: Physical 233 (2015), pp. 434–441. ISSN: 0924-4247. DOI: https://doi.org/10.1016/j.sna.2015.07.023. URL: https://www.sciencedirect.com/science/article/pii/S0924424715300777.
- [27] A. Prociak, J. Pielichowski, T. Sterzynski. "Thermal diffusivity of rigid polyurethane foams blown with different hydrocarbons". In: *Polymer Testing* 19.6 (2000), pp. 705–712. ISSN: 0142-9418. DOI: https://doi.org/10.1016/S0142-9418(99)00042-2. URL: https://www.sciencedirect.com/science/article/pii/S0142941899000422.
- [28] I. H. Bell, J. Wronski, S. Quoilin, V. Lemort. "Pure and Pseudo-pure Fluid Thermophysical Property Evaluation and the Open-Source Thermophysical Property Library CoolProp". In: *Industrial & Engineering Chemistry Research* 53.6 (2014), pp. 2498–2508. DOI: 10.1021/ie4033999. eprint: http://pubs.acs.org/doi/pdf/10.1021/ie4033999. URL: http://pubs.acs.org/doi/abs/10.1021/ie4033999.
- [29] W. Wagner, A. Pruß. "The IAPWS Formulation 1995 for the Thermodynamic Properties of Ordinary Water Substance for General and Scientific Use". In: Journal of Physical and Chemical Reference Data 31.2 (June 2002), pp. 387–535. ISSN: 0047-2689. DOI: 10.1063/1.1461829. eprint: https://pubs.aip.org/aip/jpr/article-pdf/31/2/387/16672775/387_1_online.pdf. URL: https://doi.org/10.1063/1.1461829.
- [30] National Aeronautics and Space Administration, National Oceanic and Atmospheric Administration. *U.S. Standard Atmosphere*, 1976. Tech. rep. NASA-TM-X-74335. Accessed: 2025-09-15. Washington, D.C.: NASA and NOAA, 1976. URL: https://ntrs.nasa.gov/citations/19770009539.
- [31] S. Grossmann, D. Lohse. "Scaling in thermal convection: a unifying theory". In: *Journal of Fluid Mechanics* 407 (2000), pp. 27–56. DOI: 10.1017/S0022112099007545.

- [32] R. J. A. M. Stevens, E. P. van der Poel, S. Grossmann, D. Lohse. "The unifying theory of scaling in thermal convection: the updated prefactors". In: *Journal of Fluid Mechanics* 730 (2013), pp. 295–308. DOI: 10.1017/jfm.2013.298.
- [33] E. Fonda, A. Pandey, J. Schumacher, K. R. Sreenivasan. "Deep learning in turbulent convection networks". In: *Proceedings of the National Academy of Sciences* 116.18 (2019), pp. 8667–8672. DOI: 10.1073/pnas.1900358116. eprint: https://www.pnas.org/doi/pdf/10.1073/pnas.1900358116. URL: https://www.pnas.org/doi/abs/10.1073/pnas.1900358116.
- [34] O. Shishkina, M. S. Emran, S. Grossmann, D. Lohse. "Scaling relations in large-Prandtl-number natural thermal convection". In: *Phys. Rev. Fluids* 2 (10 Oct. 2017), p. 103502. DOI: 10.1103/PhysRevFluids.2.103502. URL: https://link.aps.org/doi/10.1103/PhysRevFluids.2.103502.
- [35] P. P. Vieweg, T. Käufer, C. Cierpka, J. Schumacher. "Digital twin of a large-aspect-ratio Rayleigh-Bénard experiment: role of thermal boundary conditions, measurement errors and uncertainties". In: Flow 5 (2025), E4. DOI: 10.1017/flo.2024.35.
- [36] O. Garbrecht. "Large eddy simulation of three-dimensional mixed convection on a vertical plate". PhD thesis. Aug. 2017. DOI: 10.18154/RWTH-2018-221554.
- [37] J. Lemarechal, C. Klein, D. Puckert, U. Rist. "Application of the temperature-sensitive paint method for quantitative measurements in water". In: *Measure-ment Science and Technology* 32.10 (2021), p. 105301. DOI: 10.1088/1361-6501/ac0333. URL: https://doi.org/10.1088/1361-6501/ac0333.
- [38] J. V. Koleske. Paint and Coating Testing Manual: 15th Edition of the Gardner-Sward Handbook. ASTM International, 2012. ISBN: 978-0-8031-7017-9. DOI: 10.1520/MNL17-2ND-EB. URL: https://doi.org/10.1520/MNL17-2ND-EB.
- [39] J. Blumm, A. Lindemann. "Characterization of the thermophysical properties of molten polymers and liquids using the flash technique". In: *High Temperatures-high Pressures HIGH TEMP-HIGH PRESS* 35/36 (Jan. 2003), pp. 627–632. DOI: 10.1068/htjr144.
- [40] S. Weiss, M. S. Emran, J. Bosbach, O. Shishkina. "On temperature reconstruction from velocity fields in turbulent Rayleigh-Bénard convection". In: International Journal of Heat and Mass Transfer 242 (2025), p. 126768. ISSN: 0017-9310. DOI: https://doi.org/10.1016/j.ijheatmasstransfer.2025. 126768. URL: https://www.sciencedirect.com/science/article/pii/S0017931025001097.